SARS-CoV-2 Infects Human Engineered Heart Tissues and Models COVID-19 Myocarditis

Authors:

Adam L. Bailey[1*], Oleksandr Dmytrenko[2*], Lina Greenberg[3*], Andrea L. Bredemeyer[2], Pan Ma[2], Jing Liu[2], Vinay Penna[2], Lulu Lai[2], Emma S. Winkler[1], Sanja Sviben[4], Erin Brooks[5], Ajith P. Nair[6], Kent A. Heck[7], Aniket S. Rali[8], Leo Simpson[6], Mehrdad Saririan[9], Dan Hobohm[9], W. Tom Stump[3], James A. Fitzpatrick[4,10], Xuping Xie[11], Pei-Yong Shi[11], J. Travis Hinson[12,13], Weng-Tein Gi[14], Constanze Schmidt[14], Florian Leuschner[14], Chieh-Yu Lin[1,#], Michael S. Diamond[1,2,15,#], Michael J. Greenberg[3,#], Kory J. Lavine[1,2,16,#]

*Co-first authors
#Co-senior authors

Affiliations:

[1]Department of Pathology and Immunology, Washington University School of Medicine, St. Louis, MO, USA

[2]Department of Medicine, Washington University School of Medicine, St. Louis, MO, USA

[3]Department of Biochemistry and Molecular Biophysics, Washington University School of Medicine, St. Louis, MO, USA

[4]Washington University Center for Cellular Imaging, Washington University School of Medicine, St. Louis, MO, USA

[5]Department of Pathology & Laboratory Medicine, University of Wisconsin Hospital and Clinics, Madison, Wisconsin, USA

[6]Department of Medicine, Baylor College of Medicine, Houston, Texas, USA

[7]Department of Pathology, Baylor College of Medicine, Houston, Texas, USA

[8]Department of Medicine, Vanderbilt University, Nashville, Tennessee, USA

[9]Valleywise Health/Creighton University, Phoenix, AZ, USA

[10]Departments of Neuroscience, Cell Biology & Physiology, and Biomedical Engineering, Washington University School of Medicine, St. Louis, MO, USA

[11]Department of Biochemistry and Molecular Biology, University of Texas Medical Branch, Galveston, TX, USA

[12]Departments of Cardiology and Genetics and Genome Sciences, UConn Health, Farmington, CT.

[13]The Jackson Laboratory for Genomic Medicine, Farmington, CT

[14]Department of Internal Medicine III, University Hospital Heidelberg, University of Heidelberg, Heidelberg, Germany

[15]Department of Molecular Microbiology, Washington University School of Medicine, St. Louis, MO, USA

[16]Department of Developmental Biology, Washington University School of Medicine, St. Louis, MO, USA

Keywords: SARS-CoV-2, COVID-19, Myocarditis, Engineered Heart Tissue, Cardiomyocyte, Macrophage

45

Running Title: SARS-CoV-2 Infects Human Cardiomyocytes

47

Corresponding authors information:
Kory J. Lavine, MD, PhD
660 South Euclid Campus Box 8086
St. Louis, MO, 63110
Phone: 314 362-1171
Fax: 314 362-0186
Email: klavine@wustl.edu

Michael J. Greenberg, PhD
660 South Euclid Campus Box 8231
St. Louis, MO, 63110
Phone: 314 362-8670
Fax: 314 362-7183
Email: greenberg@wustl.edu

Michael S. Diamond, MD, PhD
660 South Euclid Campus Box 8051
Phone: 314 362-2842
Fax: 314 362-9230
Email: diamond@wusm.wustl.edu

68

69

70

71

72   **Abstract:**

73

74   Epidemiological studies of the COVID-19 pandemic have revealed evidence of cardiac

75   involvement and documented that myocardial injury and myocarditis are predictors of poor

76   outcomes. Nonetheless, little is understood regarding SARS-CoV-2 tropism within the heart and

77   whether cardiac complications result directly from myocardial infection. Here, we develop a

78   human engineered heart tissue model and demonstrate that SARS-CoV-2 selectively infects

79   cardiomyocytes. Viral infection is dependent on expression of angiotensin-I converting enzyme 2

80   (ACE2) and endosomal cysteine proteases, suggesting an endosomal mechanism of cell entry.

81   After infection with SARS-CoV-2, engineered tissues display typical features of myocarditis,

82   including cardiomyocyte cell death, impaired cardiac contractility, and innate immune cell

83   activation. Consistent with these findings, autopsy tissue obtained from individuals with COVID-

84   19 myocarditis demonstrated cardiomyocyte infection, cell death, and macrophage-predominate

85   immune cell infiltrate. These findings establish human cardiomyocyte tropism for SARS-CoV-2

86   and provide an experimental platform for interrogating and mitigating cardiac complications of

87   COVID-19.

Introduction:

88

89   Severe Acute Respiratory Syndrome Coronavirus 2 (SARS-CoV-2) is the cause of the

90   ongoing Coronavirus Disease-2019 (COVID-19) pandemic. Since its emergence in Wuhan, China

91   in late 2019, SARS-CoV-2 has infected millions of people worldwide, overwhelmed the capacity

92   of healthcare systems, and continues to result in unacceptably high mortality rates. Although most

93   severe cases of COVID-19 are characterized by respiratory distress, the disease has a highly

94   variable clinical course with myriad manifestations. Epidemiological studies have identified pre-

95   existing cardiovascular disease as a strong risk factor for the development of severe COVID-19

96   and mortality (reviewed in[1]). Cardiovascular manifestations of COVID-19 including elevated

97   troponin, reduced left ventricular systolic function, and arrhythmias are consistent with

98   cardiomyocyte injury. Cardiac complications occur in 20-44% of hospitalized patients, and

99   constitute an independent risk factor for COVID-19 mortality[1–4]. Cardiac MRI studies have

100   suggested that persistent myocardial injury may be more common than appreciated and occur in

101   less severe forms of COVID-19[5–7]. The mechanistic basis by which SARS-CoV-2 results in

102   cardiac dysfunction remains obscure. It remains unknown whether these effects are a result of

103   direct viral infection of cardiac cells or a systemic inflammatory response to extracardiac

104   infection[8]. If direct infection does contribute to COVID-19-associated cardiac injury, defining the

105   cell-types susceptible to infection will be important for understanding COVID-19 cardiac

106   pathogenesis and devising effective treatment strategies.

107   It has been challenging to study the cardiac manifestations of COVID-19. Obtaining

108   cardiac tissue from critically ill patients with suspected COVID-19 myocarditis poses unique

109   challenges. Furthermore, there are few animal models to study cardiovascular complications

110   observed in SARS-CoV-2 infected humans[9]. The most commonly used laboratory animal model,

111   the mouse, is not susceptible to SARS-CoV-2 infection due to poor affinity of the viral spike protein

112   for the murine ACE2 receptor[10,11], and systems that enable expression of human ACE2 from cells

113   in the murine cardiovascular system are not yet widely available. Therefore, there is a critical need

4

114   to develop robust model systems that enable the investigation of the cardiovascular complications

115   of COVID-19.

116   Human engineered heart tissues (EHTs) provide unique advantages as model systems

117   for studying COVID-19 cardiac pathology. EHTs are self-assembled using defined cellular and

118   extracellular matrix compositions. EHTs generate contractile force, display electrical coupling,

119   and have cellular organization that mimics myocardial tissue (reviewed in[12,13]). Human EHTs can

120   be formed from human pluripotent stem cell (hPSC)-derived cardiomyocytes, where the three-

121   dimensional environment of the EHT promotes the maturation of these cells[14].

122   Here, we devised an EHT model of COVID-19 myocarditis and tested the hypothesis that

123   SARS-CoV-2 promotes cardiac pathology by infecting cardiomyocytes and activating local

124   immune responses. We demonstrate that SARS-CoV-2 selectively infects and replicates within

125   hPSC-derived cardiomyocytes, ultimately resulting in cardiomyocyte cell death. We provide

126   evidence that cardiomyocyte infection is dependent on ACE2 expression and endosomal cysteine

127   protease activity. SARS-CoV-2-infected EHTs displayed typical features of myocarditis, including

128   activation of immune cells, decreased contractile force generation, and cardiomyocyte cell death.

129   Furthermore, autopsy and biopsy samples from four patients with confirmed SARS-CoV-2

130   infection and clinical myocarditis demonstrated patchy cardiomyocyte infection that was

131   accompanied by myocardial cell death and macrophage accumulation. These findings

132   demonstrate that SARS-CoV-2 can productively infect human cardiomyocytes and establish

133   EHTs as a platform for mechanistic investigation of COVID-19 myocarditis.

134   **Results:**

135   **ACE2 is expressed in human cardiomyocytes**

136   To explore whether human cardiomyocytes might be susceptible to SARS-CoV-2

137   infection, we examined the expression of angiotensin converting enzyme 2 (ACE2) within the

138   human heart. Previous studies have established that ACE2 serves as a cell-surface receptor for

139   SARS-CoV-2 through interactions with the spike protein in numerous human cell types[15,16].

140   Immunostaining of human left ventricular myocardial tissue revealed evidence of ACE2

141   expression in cardiomyocytes (**Fig. 1a**). We observed significant variation in ACE2 expression

142   between individual cardiomyocytes within the same myocardial specimen. ACE2 mRNA was

143   abundantly expressed in the healthy human heart and further increased in the context of chronic

144   heart failure (**Fig. 1b)**. RNA sequencing of human pediatric and adult heart failure specimens

145   revealed robust expression of ACE2 mRNA within the human heart across the spectrum of age

146   (**Fig. 1c**). Consistent with our immunostaining findings, primary human cardiomyocytes obtained

147   from the left ventricle and atria expressed ACE2 mRNA (**Fig. 1d**). These data are consistent with

148   prior single cell and bulk RNA sequencing analyses of human myocardium and suggest that

149   cardiomyocytes might be permissive to SARS-CoV-2 infection[17].

150   To ascertain whether human pluripotent stem cell-derived cardiomyocytes (hPSC-derived

151   CMs) can serve as an appropriate model to study cardiac SARS-CoV-2 infection, we measured

152   ACE2 mRNA expression in hPSC-derived CMs. Quantitative RT-PCR revealed that hPSC-

153   derived CMs abundantly expressed ACE2 mRNA. In contrast, minimal ACE2 mRNA was detected

154   in human dermal fibroblasts, hPSC-derived cardiac fibroblasts, or human fetal cord blood derived-

155   macrophages (**Fig. S1a-c**). Human engineered heart tissues (EHTs) self-assembled between two

156   deformable polydimethylsiloxane (PDMS) posts after mixing cells in an extracellular matrix

157   composed of collagen and matrigel (**Fig. S1d**). EHTs composed of either hPSC-derived CMs and

158   fibroblasts or hPSC-derived CMs, fibroblasts, and macrophages also expressed ACE2 mRNA

159   (**Fig. S1e**). Immunostaining of EHTs confirmed the presence of ACE2 protein specifically in

6

160   hPSC-derived CMs (**Fig. S1f**). These data suggest that hPSC-derived CMs might be susceptible

161   to SARS-CoV-2 infection and serve as a suitable experimental model to study cardiac

162   manifestations of COVID-19.

163

164   **SARS-CoV-2 infects hPSC-derived cardiomyocytes**

165   To determine the susceptibility of different myocardial cell types to SARS-CoV-2 infection,

166   we inoculated various stromal populations with a recombinant SARS-CoV-2 clone containing a

167   NeonGreen fluorescent reporter (SARS-CoV-2-mNeonGreen)[18]. NeonGreen is expressed from a

168   viral subgenomic RNA, indicative of active viral replication. We were unable to detect infection of

169   primary human cardiac fibroblasts, endothelial cells, or macrophages (**Fig. 1e,** gating schemes:

170   **Fig. S2**). hPSC-derived endothelial cells and cardiac fibroblasts were also not susceptible to

171   infection (**Fig. S1g**). In contrast, two independent lines of hPSC-derived cardiomyocytes (hPSC-

172   derived CMs) were permissive to SARS-CoV-2 infection (**Fig. 1f**). Undifferentiated hPSC lines did

173   not demonstrate evidence of infection (**Fig S3**).

174   To confirm cardiomyocyte tropism, we inoculated various combinations of hPSC-derived

175   CMs, fibroblasts, and macrophages grown in monolayer culture with wild-type SARS-CoV-2

176   (USA_WA1/2019). We analyzed tissue culture supernatants for production of infectious virus

177   using a Vero cell infection-based focus forming assay, and we measured intracellular viral RNA

178   transcript levels using RT-qPCR at 3 days post-inoculation. These assays revealed the production

179   of infectious virus (**Fig. 2a**) and viral RNA (**Fig. 2b**) selectively in cultures that contained hPSC-

180   derived CMs. Cultures lacking hPSC-derived CMs contained viral loads that were equivalent to

181   media-only controls. A time course of hPSC-derived CM infection showed that cardiomyocytes

182   rapidly produced infectious virus with peak titers observed at day 3 post-inoculation. These

183   kinetics were closely mirrored by SARS-CoV-2-mNeonGreen (**Fig. 2c**).

184   Using SARS-CoV-2-mNeonGreen, we examined the relationship between viral replication

185   and cell death using flow cytometry. Although the percentage of hPSC-derived CMs that were

186   mNeonGreen-positive peaked at day 3 post-inoculation, significant levels of hPSC-derived CM

187   cell death were not observed until 4-5 days post-inoculation (**Fig. 2d**) indicating that viral infection

188   precedes hPSC-derived CM cell death. SARS-CoV-2-infected cardiomyocytes also displayed

189   characteristics of cytopathic effects. Cellular rounding, clumping, and syncytium formation first

190   were observed on day 3 post-inoculation. Distortion of cellular morphology was evident by day 4

191   post-inoculation and cultures contained largely dead cells and debris by days 5-6 post-inoculation

192   (**Fig. 2e**).

193   To verify that cardiomyocytes are the primary target of SARS-CoV-2 in a simulated cardiac

194   environment, we infected two-dimensional tissues assembled with hPSC-derived CMs (80%),

195   fibroblasts (10%), and macrophages (10%) with SARS-CoV-2-mNeonGreen. Flow cytometry

196   performed 3 days following infection revealed mNeonGreen expression only in CD90$^-$CD14$^-$

197   TNNT2$^+$ cardiomyocytes. mNeonGreen was not detected in CD90$^+$ fibroblasts or CD14$^+$

198   macrophages within infected two-dimensional tissues (**Fig. 2f-g, Fig. S4**). These data

199   demonstrate selective viral tropism in cardiomyocytes. Consistent with this conclusion,

200   transmission electron microscopy of infected two-dimensional tissues performed 3 days post-

201   inoculation demonstrated the presence of coronavirus particles within infected hPSC-derived

202   CMs. Micrographs revealed structural features of coronaviruses including the presence of a tri-

203   laminar envelope and characteristic cross-sections through the nucleocapsid[19,20] (**Fig. 2h**). Virions

204   were identified within perinuclear endosomal-like structures of hPSC-derived CMs. We observed

205   various stages of virion assembly including budding from intracellular membranes. Virions were

206   not detected in mock-infected cardiomyocytes.

207

208   **RNA sequencing identified robust viral transcription and the activation of innate immune**

209   **responses in hPSC-derived cardiomyocytes and two-dimensional tissues**

210   To examine viral transcription and the host immune response to SARS-CoV-2 infection,

211   we performed RNA sequencing. Cultures containing either hPSC-derived CMs, fibroblasts, or

8

212   macrophages were either mock-infected or inoculated with SARS-CoV-2. We also examined two-

213   dimensional co-culture tissues assembled with 80% cardiomyocytes, 10% fibroblasts, and 10%

214   macrophages. Cells and tissues were harvested on day 3 post-inoculation. Principal component

215   analysis revealed separation between experimental groups consistent with their distinct cellular

216   composition (**Fig. 3a**). Classification of transcript types demonstrated that infected hPSC-derived

217   CMs and two-dimensional tissues comprised of hPSC-derived CMs and fibroblasts or hPSC-

218   derived CMs, fibroblasts, and macrophages contained abundant viral transcripts (**Fig. S5a**). We

219   then assessed the expression of specific viral transcripts by aligning the RNA sequencing data to

220   the SARS-CoV-2 genome and transcriptome. Subgenomic RNAs were identified based on the

221   presence of 5' leader sequences[21]. We observed robust expression of most SARS-CoV-2

222   genomic and subgenomic RNAs in infected hPSC-derived CMs and two-dimensional tissues with

223   the exception of ORF7b (**Fig. 3b, Fig. S5b**).

224   To facilitate differential expression analysis of host genes, we censored viral RNAs from

225   the RNA sequencing computational model. This was necessary given the asymmetric prevalence

226   of viral transcripts across samples. We identified numerous host genes that were differentially

227   regulated upon SARS-CoV-2 infection in each of the examined cell types and two-dimensional

228   tissues (**Fig. 3c**). Conditions that supported viral replication (hPSC-derived CMs and two-

229   dimensional tissues) displayed the greatest overlap in differentially expressed genes. Cell types

230   that did not support viral replication (fibroblasts and macrophages) also demonstrated numerous

231   differentially expressed host genes, indicating that SARS-CoV-2 might elicit changes in host gene

232   expression in the absence of direct viral infection. Notably, host genes differentially expressed in

233   fibroblasts and macrophages exposed to SARS-CoV-2 were largely distinct (**Fig. 3d**). These

234   findings suggest that elements within or on the surface of SARS-CoV-2 virions may serve as

235   pathogen-associated molecular patterns (PAMPs) and stimulate distinct gene expression

236   programs in differing cell types.

237   GO pathway analysis revealed that infected hPSC-derived CMs and two-dimensional co-

238   culture tissues showed upregulation of genes associated with immune cell activation, stress-

239   induced transcription, and responses to pathogens including viruses. Genes associated with

240   metabolism, oxidative phosphorylation, and mitochondrial function were downregulated by

241   infection. Two-dimensional tissues displayed alterations in other pathways including upregulation

242   of cellular responses to cytokines and downregulation of genes involved in muscle contraction

243   (**Fig. 3e-f**). Host genes differentially expressed in macrophages and fibroblasts were associated

244   with pathways involved in innate immune cell activation, migration, and cytokine responses (**Fig.**

245   **3g-h**).

246   Examination of specific genes differentially regulated in infected hPSC-derived CMs and

247   two-dimensional tissues (**Fig. 3i**) revealed marked reduction in components of the electron

248   transport chain (ATP synthase, mitochondrial cytochrome C oxidase, NADPH dehydrogenase)

249   and key upstream metabolic regulators (glycerol-3-phosphate dehydrogenase, pyruvate

250   dehydrogenase, succinate dehydrogenase complex). *PDK4*, an inhibitor of pyruvate

251   dehydrogenase was upregulated in infected hPSC-derived CMs and two-dimensional tissues. We

252   also observed marked downregulation of numerous components and regulators of the contractile

253   apparatus including cardiac actin, troponin subunits, myosin light and heavy chains, desmin,

254   phospholamban, and calsequestrin in infected two-dimensional tissues. Infected hPSC-derived

255   CMs displayed similar changes, albeit to a lesser extent. *ACE2* expression was diminished in

256   infected cardiomyocytes and two-dimensional tissues.

257   Infected hPSC-derived CMs and two-dimensional tissues also displayed upregulation of

258   key regulators of innate immunity (**Fig. 3i**). Type I interferon (IFN) activation was apparent by the

259   increased expression of *IFNB1* and numerous IFN stimulated genes including *IFIT1*, *IFIT2*, *IFIT3*,

260   *ISG15*, *MX1*, and *OAS1*. Stress response programs (FOS) and cytokine expression (TNF) were

261   similarly upregulated in these cell types. Consistent with a greater innate immune response in

262   two-dimensional tissues, we found that several chemokines (*CCL3*, *CCL4*, *CCL7*, *CCL8*, and

263   *CXCL8*) and cytokines (*IL1B*, *IL6*, and *CSF3*) were selectively upregulated in infected two-

264   dimensional tissues. Macrophages and fibroblasts contributed to enhanced chemokine and

265   cytokine responses in two-dimensional tissues. *CCL3*, *CCL4*, and *CCL8* were selectively

266   expressed in infected macrophages and *CSF3*, *CXCL8*, *IL1B*, and *IL6* were induced in infected

267   fibroblasts (**Fig. S5c**).

268

269   **SARS-CoV-2 entry into hPSC-derived cardiomyocytes is mediated by ACE2 and**

270   **endosomal cysteine proteases**

271   To elucidate the mechanism(s) by which SARS-CoV-2 enters cardiomyocytes, we

272   examined SARS-CoV-2 infection of hPSC-derived CMs in the presence of well-established entry

273   inhibitors. ACE2 serves as the cell-surface receptor for SARS-CoV-2 in humans[15,16]. Blockade of

274   ACE2 with anti-hACE2 antibody abrogated SARS-CoV-2-NeonGreen infectivity in hPSC-derived

275   CMs as measured by NeonGreen-positivity and viral RNA extracted from the supernatant of

276   infected cultures. The extent of blockade was comparable to treatment with remdesivir, a potent

277   inhibitor of the SARS-CoV-2 RNA-dependent RNA polymerase[22–24] (**Fig. 4a-b**).

278   After binding to ACE2, the SARS-CoV (and SARS-CoV-2) spike protein must undergo

279   proteolytic activation to initiate membrane fusion[25]. Host proteases located at the plasma

280   membrane (TMPRSS2) or within endosomes (cathepsins) most commonly perform this function.

281   The relative contributions of each of these protease families to SARS-CoV-2 infection varies by

282   cell-type[15,25]. RNA sequencing data revealed that hPSC-derived CMs express robust levels of

283   ACE2 and multiple endosomal proteases including cathepsins and calpains (**Fig. 4c**). ACE2

284   mRNA was not abundantly expressed in either macrophages or fibroblasts. While TMPRSS2

285   expression was present at the lower limit of detection for RNAseq, we detected low, but

286   measurable levels of TMPRSS2 by RT-qPCR in hPSC-derived CMs, but not in fibroblasts or

287   macrophages (**Fig. 4c-d**).

11

288   To determine whether SARS-CoV-2 enters cardiomyocytes through an endosomal or

289   plasma membrane route, we inoculated hPSC-derived CMs with SARS-CoV-2-mNeonGreen and

290   administered either the endosomal cysteine protease inhibitor E-64, which blocks cathepsins, or

291   the serine protease inhibitor camostat mesylate, which blocks TMPRSS2 (and possibly

292   TMPRSS4) [25]. Notably, E-64 abolished SARS-CoV-2 infection of hPSC-derived CMs as

293   demonstrated by reduced mNeonGreen expression and viral RNA within the supernatant (**Fig.**

294   **4e-f**). In contrast, camostat had no effect on cardiomyocyte infection over a range of doses (**Fig.**

295   **4g-h**). Thus, SARS-CoV-2 enters cardiomyocytes through an endosomal pathway that requires

296   cathepsin but not TMPRSS2-mediated cleavage.

297

298   **EHTs model COVID-19 myocarditis**

299   Myocarditis is characterized by direct viral infection of cardiomyocytes and accumulation

300   of immune cells at sites of active infection or tissue injury[26,27]. To examine whether SARS-CoV-2

301   infection of cardiomyocytes in a three-dimensional environment mimics aspects of viral

302   myocarditis, we generated EHTs containing either hPSC-derived CMs and fibroblasts or hPSC-

303   derived CMs, fibroblasts, and macrophages. EHTs were seeded in a collagen-Matrigel matrix

304   between two PDMS posts, infected with SARS-CoV-2, and harvested 5 days after inoculation.

305   Hematoxylin and eosin (H&E) staining revealed evidence of tissue injury and increased interstitial

306   cell abundance within the periphery of SARS-CoV-2-infected EHTs (**Fig. 5a**). Immunostaining for

307   the viral nucleocapsid protein demonstrated evidence of prominent infection at the periphery of

308   the EHT. Nucleocapsid staining was localized within hPSC-derived CMs. Staining for CD68

309   demonstrated macrophage accumulation corresponding to sites of interstitial cell accumulation

310   and viral infection (**Fig. 5b, Fig. S6**). Enrichment of nucleocapsid staining at the periphery of the

311   tissue suggests that viral diffusion might be limited by the three-dimensional EHT environment.

312   Consistent with our immunostaining results, infected EHTs (with and without macrophages)

313   accumulated high levels of viral RNA, as detected by quantitative RT-PCR (**Fig. 5c**). *In situ*

314   hybridization for viral spike sense and antisense RNA was also indicative of viral replication within

315   EHTs (**Fig. 5d, Fig. S7**).

316

317   **SARS-CoV-2 infection causes contractile dysfunction and cell death**

318   Reduced left ventricular systolic function has been reported in severe cases of COVID-19

319   myocarditis[28]. Therefore, we examined the effect of SARS-CoV-2 infection on cardiomyocyte

320   contractile function in EHTs. EHTs were seeded between two deformable PDMS posts of known

321   stiffness. As the tissue contracts, it displaces the posts, and by tracking the displacement of the

322   posts as a function of time, we calculated the speed of contraction and relaxation. The average

323   peak displacement was calculated for each spontaneously contracting tissue over the course of

324   at least 60 seconds (**Supplemental Movies 1-2**).

325   EHTs consisting of hPSC-derived CMs and fibroblasts were assembled and allowed to

326   mature for 7 days prior to infection. EHTs were inoculated with SARS-CoV-2, and contractile

327   function was analyzed daily. From days 0 to 3 post infection, the average maximal displacement

328   generated during beating did not differ between the mock and SARS-CoV-2-infected tissues.

329   However, on days 4 to 5 post infection, the SARS-CoV-2 inoculated tissues showed reduced

330   contraction relative to the mock-infected tissues (**Fig. 5e-f**). On day 5 after inoculation, the

331   maximal displacement produced during contraction by the SARS-CoV-2 inoculated tissues was

332   markedly lower than mock infected-tissues. Moreover, the tissues show reduced speed of

333   contraction and relaxation, consistent with systolic dysfunction (**Fig. 5g**).

334

335   **Mechanisms of reduced EHT contractility**

336   To examine whether cardiomyocyte cell death might serve as a mechanism explaining

337   reduced EHT contractility on days 4 to 5 post inoculation, we performed TUNEL staining.

338   Consistent with the temporal course of SARS-CoV-2 cardiomyocyte infection and cell death in

339   our two-dimensional hPSC-CM cultures (**Fig. 2d**), we observed increased numbers of TUNEL

340   positive cardiomyocytes in SARS-CoV-2 infected EHTs on day 5 post infection (**Fig. 6a-b**). Our

341   RNA sequencing data suggest that other mechanisms also may contribute to reduced EHT

342   contractility, including decreased expression of genes important for sarcomere function and

343   metabolism as well as activation of host immune responses (**Fig. 3i**). Consistent with the

344   possibility that disrupted sarcomere gene expression might contribute to reduced EHT

345   contractility, immunostaining of hPSC-derived CMs infected with SARS-CoV-2 revealed evidence

346   of sarcomere loss 3 days following infection (**Fig. 6c**), a time point that preceded cell death.

347   Furthermore, immunostaining of EHTs demonstrated loss of Troponin T expression in infected

348   cardiomyocytes. (**Fig. 6d-e**). Thus, the reduction in contractile function may be multifactorial with

349   contributions from virus-induced cardiomyocyte cell death and loss of sarcomere elements.

350   We then examined the mechanistic relationship between cardiomyocyte infection,

351   inflammatory signaling, sarcomere breakdown, and cell death. Inhibition of viral entry (ACE2

352   neutralizing antibody) or viral replication (remdesivir) was sufficient to prevent type I IFN and TNF

353   expression following SARS-CoV-2 infection (**Fig. 6f-g**). Remdesivir similarly reduced

354   inflammatory gene expression in 3D EHTs (**Fig. S8a-b**). These data establish that viral infection

355   represents the upstream driver of inflammation in our model system.

356   To examine the impact of cardiomyocyte inflammatory signaling on cardiomyocyte cell

357   death, sarcomere gene expression, and sarcomere structure, we focused on inhibiting viral

358   nucleic acid sensing. TBK1 (TANK-binding kinase 1) is an essential mediator of numerous nucleic

359   acid sensing pathways including RIG-I, MAVS, STING, and TLRs [29,30]. Inhibition of TBK1 activity

360   was sufficient to reduce type I IFN activity (primary inflammatory signature identified in infected

361   cardiomyocytes, **Fig 3i**) without impacting viral load or cardiomyocyte infectivity (**Fig. 6f-h**).

362   Inhibition of TBK1 activity during SARS-CoV-2 cardiomyocyte infection had no impact on

363   cardiomyocyte cell death (**Fig. 6i**). While TBK1 inhibition prevented reductions in TNNT2 and

364   MYH7 mRNA expression following cardiomyocyte SARS-CoV-2 infection, sarcomere breakdown

365   remained prevalent in infected cardiomyocytes treated with the TBK1 inhibitor. In contrast,

14

366   remdesivir prevented both reductions in TNNT2 and MYH7 mRNA expression and sarcomere

367   loss following SARS-CoV-2 infection (**Fig. 6j-k, Fig. S8c-d)**. These data indicate that SARS-CoV-

368   2 elicits an inflammatory response in cardiomyocytes that is at least partially dependent on viral

369   nucleic acid sensing and TBK1 signaling. However, TBK1-dependent cardiomyocyte

370   inflammation does not appear responsible for sarcomeric disassembly or cardiomyocyte cell

371   death. These findings do not rule out the possibility that other inflammatory pathways or cross-

372   talk between infected cardiomyocytes and immune cells contributes to reduced EHT contractility.

373

374   **Evidence of cardiomyocyte infection in COVID-19 myocarditis**

375   To validate the myocarditis phenotype generated by SARS-CoV-2 infection of the EHT

376   model, we obtained autopsy and endomyocardial biopsy specimens from four subjects with

377   confirmed SARS-CoV-2 infection and clinical diagnoses of myocarditis. Evidence of myocardial

378   injury (elevated troponin) and left ventricular systolic dysfunction were present in each case

379   (**Table 1**). Coronary angiography demonstrated no evidence of luminal stenosis or thrombosis.

380   The presence of SARS-CoV-2 RNA from nasopharyngeal samples was confirmed by clinical

381   diagnostic testing or post-mortem.

382   Postmortem microscopic examination of the left ventricular myocardium demonstrated

383   areas of cardiomyocyte necrosis and degenerative vacuolization of cardiomyocyte cytoplasm

384   were noted accompanied by a mixed mononuclear cell infiltrate (**Fig. 7a**). These changes are

385   distinct from postmortem autolytic changes. Examination of the coronary arteries from the COVID-

386   19 myocarditis autopsy cases demonstrated non-obstructive mild atherosclerotic changes,

387   consistent with the angiogram findings. There was no evidence of microvascular injury or

388   thromboembolic events. Two autopsy heart samples from subjects with metastatic carcinoma and

389   an inherited neurodegenerative disease with similar tissue procurement times were included as

390   negative controls.

15

391   RNA *in situ* hybridization for SARS-CoV-2 spike and nucleocapsid genes revealed

392   evidence of viral RNA within the myocardium of each COVID-19 myocarditis subject. Viral

393   transcripts were located in cytoplasmic and perinuclear locations within cells that were

394   morphologically consistent with cardiomyocytes (**Fig. 7b, Fig. S9a-b**). Viral transcripts also were

395   identified in airway epithelial cells within the lung of this subject and other myocardial cell types

396   including perivascular adipocytes and pericytes (**Fig. S9c**). Immunostaining for the nucleocapsid

397   protein further demonstrated presence of viral protein in cardiomyocytes **Fig. 7c**). The COVID-19

398   myocarditis immune cell infiltrate was characterized by accumulation of a mixed population of

399    $CCR2^-$ and $CCR2^+$ macrophages within injured areas of the myocardium (**Fig. 7d**). Minimal

400   evidence of T-cell infiltration was noted (**Fig. 7e**). Macrophage abundance was highest in areas

401   that demonstrated evidence of cardiomyocyte injury as depicted by complement deposition (C4d

402   staining), a pathological marker of cardiomyocyte cell death[31–33] (**Fig. S9d**). Together, these

403   observations provide initial pathological evidence that SARS-CoV-2 infects the human heart and

404   may contribute to cardiomyocyte cell death and myocardial inflammation that is distinct from

405   lymphocytic myocarditis.

406

407 **Discussion:**

408   Cardiac manifestations of COVID-19 including myocardial injury (elevated troponin),

409 reduced left ventricular systolic function, and arrhythmias are increasingly recognized as

410 important determinants of morbidity and mortality[3,8]. Moreover, imaging studies have uncovered

411 evidence of chronic myocardial pathology among both hospitalized and ambulatory patients,

412 suggesting the potential for long-term consequences of COVID-19[5,6]. Little is understood

413 regarding the etiology of these conditions. To gain insight into the cardiac complications of

414 COVID-19, we developed a human EHT system that recapitulates many features of SARS-CoV-

415 2 induced myocarditis. We provide evidence that SARS-CoV-2 infects hPSC-derived CMs,

416 resulting in reduced metabolic and contractile apparatus gene expression, sarcomeric

417 disassembly, inflammatory signaling, and cell death. Viral entry was ACE2-dependent and relied

418 on endosomal cysteine protease activity. Our findings are consistent with a recent report

419 suggesting that SARS-CoV-2 infects human cardiac slices and hPSC-derived CMs in an ACE2

420 and cathespin dependent manner[34]. We extend these observations to show that cardiomyocytes

421 supported viral replication, rapidly produced infectious virions, activated type I IFN signaling, and

422 displayed cytopathic features seen with coronavirus infection. Infected EHTs demonstrated

423 reduced contractile force, sarcomere disassembly, and pathological evidence of myocarditis

424 including macrophage activation. Examination of human autopsy and endomyocardial biopsy

425 tissue from individuals diagnosed with COVID-19 myocarditis revealed similar findings of

426 cardiomyocyte infection, cell death, and macrophage infiltration.

427   Whether cardiac manifestations of COVID-19 are a result of viral infection or exuberant

428 systemic inflammation remains a debated topic. It is also possible that microvascular thrombosis

429 may contribute to cardiac events. We provide evidence that SARS-CoV-2 readily infects and

430 replicates within human cardiomyocytes, indicating that viral infection likely contributes to the

431 pathogenesis of COVID-19 myocarditis. SARS-CoV-2 was unable to replicate in other cell types

432 found within the left ventricular myocardium including cardiac fibroblasts, endothelial cells, and

17

433   macrophages. It remains possible that SARS-CoV-2 could also infect other cardiac cell types that

434   are difficult to isolate from the human heart or produce through directed differentiation protocols,

435   such as pericytes and endocardial cells. Despite these limitations, our findings clearly

436   demonstrate that cardiomyocytes are a target of SARS-CoV-2 infection.

437   Consistent with this conclusion, examination of human autopsy and endomyocardial

438   biopsy tissue obtained from four patients with clinical diagnoses of COVID-19 myocarditis

439   revealed evidence of myocardial SARS-CoV-2 RNA and protein predominately within

440   cardiomyocytes and accumulation of macrophages in areas surrounding myocardial injury. These

441   findings are consistent with prior reports highlighting infiltration of monocytes, lymphocytes, and

442   plasma cells in an endomyocardial biopsy specimen from a patient with suspected COVID-19

443   myocarditis[35] and viral RNA within the myocardium of COVID-19 autopsy specimens[36]. It is

444   important to note that the human specimens examined in this study differ substantially from

445   published autopsy series that did not include subjects with cardiac manifestations [3,37]. Here, we

446   exclusively focused on subjects with active COVID-19 infection and clinical evidence of

447   myocarditis based on echocardiography and clinical presentation.

448   Numerous studies have reported that extrapulmonary cell types are susceptible to SARS-

449   CoV-2 infection[38–40]. This broader cellular tropism appears to be dictated by ACE2 expression

450   and the ability of the virus to gain access to extrapulmonary tissues. Among cell types within the

451   heart, cardiomyocytes and pericytes express ACE2 mRNA[17]. Our immunostaining studies of

452   human heart samples and EHTs suggest that ACE2 protein is most prominently expressed in

453   cardiomyocytes. Using a human ACE2 neutralizing antibody, we demonstrated that ACE2 is

454   essential for SARS-CoV-2 to infect cardiomyocytes. It is not yet clear at what stage during the

455   course of their differentiation developing cardiomyocytes become permissive to SARS-CoV-2

456   infection. Furthermore, it remains to be explored whether cardiomyocyte maturation, remodeling,

457   and/or subset diversification might impact vulnerability or host responses to viral infection. This

458   possibility is supported by the heterogeneous expression of ACE2 in the human heart and hPSC-

18

459   derived CMs, and may explain why pre-existing cardiovascular disease represents such a strong

460   risk factor for COVID19 mortality. Consistent with this idea, ACE2 expression is increased in heart

461   failure[28,41]. hPSC-derived CMs and EHTs offer an opportunity to address these important

462   questions. Indeed, a previous study demonstrated that hPSC-derived cells (including

463   cardiomyocytes) can support SARS-CoV-2 infection[40]. Whether SARS-CoV-2 enters the heart

464   through hematological seeding and/or direct extension from the pleural cavity remains unknown.

465   Emerging data suggests that SARS-CoV-2 can enter cells either directly through the

466   plasma membrane using TMPRSS2 or through endosomal pathways via cathepsins, and that the

467   utilization of these pathways is cell-type dependent[15,16]. We demonstrate that SARS-CoV-2

468   depends almost exclusively upon the endosomal pathway for entry into hPSC-derived CMs, which

469   is consistent with the greater abundance of transcripts for endosomal cathepsins relative to

470   TMPRSS2 and TMPRSS4 transcripts. As such, hPSC-derived CMs may be informative for the

471   development and testing of drugs that target viral cell entry. Based on this, we predict that

472   compounds targeting endosomal viral entry would have greater efficacy in preventing COVID-19

473   cardiac infection than those targeting TMPRSS2 or related proteases.

474   EHTs provided an opportunity to gain mechanistic insights into the relationship between

475   cardiomyocyte infection, myocardial inflammation, and contractile dysfunction. Infection of EHTs

476   resulted in generation of inflammatory mediators, reduced ACE2 expression, cardiomyocyte cell

477   death, disrupted sarcomeric structure, and changes in sarcomeric and metabolic gene

478   expression. Each of these mechanisms likely contribute to reduced EHT contractility. We

479   demonstrated that cardiomyocyte infection is essential for inflammatory gene expression,

480   sarcomere loss, and cell death. Intriguingly, blockade of viral nucleic acid sensing pathways

481   (TBK1 inhibitor) blunted reductions in sarcomere gene expression. However, sarcomere

482   disassembly in infected cells and cardiomyocyte cell death was not impacted. These findings

483   highlight the central role of cardiomyocyte infection and suggest that targeting pathways that are

484   responsible for sarcomere breakdown may improve outcomes in patients with cardiac

19

485 complications of COVID-19. However, our findings do not exclude an important role for

486 inflammation in COVID-19 myocarditis. The relevance of ACE2 downregulation in infected

487 cardiomyocytes will require further clarification as $Ace2^{-/-}$ mice display left ventricular systolic

488 dysfunction and heart failure[42].

489   Effectively targeting the inflammatory response to SARS-CoV-2 infection in the heart will

490 require a careful dissection of the cell types involved and identification of key effector pathways.

491 Macrophages and fibroblasts appear to contribute to the inflammatory response. Despite low

492 levels of ACE2 expression and resistance to SARS-CoV-2 infection, macrophages and fibroblasts

493 each generated inflammatory chemokines and cytokines in response to exposure to SARS-CoV-

494 2 in 2D culture, a response likely driven by recognition of viral RNAs and/or proteins. The addition

495 of fibroblasts and macrophages to 2D engineered heart tissues exaggerated production of

496 immune-related mRNAs following exposure to SARS-CoV-2. While this response could be a

497 result of direct recognition of viral RNAs and proteins by fibroblasts and macrophages, additional

498 mechanisms of macrophage and fibroblast activation should be considered such as

499 communication between infected cardiomyocytes and adjacent macrophages and fibroblasts

500 through either the production of soluble mediators or intercellular transfer via gap junctions. Future

501 studies are necessary to dissect the cellular mechanisms and signaling pathways that initiate and

502 potentiate local inflammation between infected cardiomyocytes and surrounding macrophages,

503 fibroblasts, and other cell types.

504   EHTs have been considered as models for dilated and hypertrophic cardiomyopathies

505 given their genetic etiologies[43,44]. Here, we developed a human EHT model of viral myocarditis.

506 EHTs infected with SARS-CoV-2 recapitulated several features of viral myocarditis including

507 cardiomyocyte infection, cell death, inflammation, and contractile dysfunction. These EHTs

508 contained hPSC-derived CMs, monocyte-derived macrophages, and fibroblasts to mirror some of

509 the cellular and extracellular constituents of the human myocardium. To our knowledge,

510 macrophages have not been previously incorporated into human EHTs. Given recent advances

20

511   in stem cell differentiation protocols, incorporation of tissue resident macrophages, endothelial

512   cells, and cardiac fibroblasts is on the horizon and could further strengthen this model system[45,46].

513   Moreover, it is possible to genetically modify each of these cellular components to gain

514   mechanistic insights into the pathogenesis of various diseases including COVID-19 myocarditis.

515   These observations add to an emerging field that have successfully utilized EHT systems for

516   testing of compounds for cardiotoxicity and efficacy[47,48]. From a broader perspective, our findings

517   are consistent with the emerging utility of human organoid systems in the investigation of SARS-

518   CoV-2[38,39,49,50].

519   Our study is not without limitations, including limited autopsy and biopsy tissue availability,

520   inherent immaturity of hPSC-derived CMs, and incomplete representation of human myocardial

521   cell types included in EHTs. Nonetheless, our experiments support the conclusion that SARS-

522   CoV-2 infection of cardiomyocytes and resultant myocardial injury and inflammation likely

523   promote or contribute to cardiac manifestations. We provide evidence that human EHTs

524   recapitulate many features of COVID-19 myocarditis, demonstrate that SARS-CoV-2 infection of

525   EHTs can produce multiscale changes spanning from the molecular to functional levels, and show

526   that EHTs serve as useful tools for dissecting mechanisms that contribute to cardiac pathology.

527

528 **Methods:**

529

530 **_Biosafety._** All aspects of this study were approved by the office of Environmental Health and

531 Safety at Washington University School of Medicine prior to the initiation of this study. Work with

532 SARS-CoV-2 was performed in a BSL-3 laboratory by personnel equipped with powered air

533 purifying respirators (PAPR).

534

535 **_Viruses._** The 2019n-CoV/USA_WA1/2019 isolate of SARS-CoV-2 was obtained from the United

536 States Centers for Disease Control (CDC). The mNeonGreen SARS-CoV-2 virus was published

537 recently [18]. Infectious stocks were grown by inoculating Vero CCL81 cells and collecting

538 supernatant upon observation of cytopathic effect. Debris was removed by centrifugation and

539 passage through a 0.22 µm filter. Supernatant was then aliquoted and stored at -80°C. All

540 infections were performed at a multiplicity of infection (MOI) of 0.1. The mNeonGreen SARS-CoV-

541 2 virus stock used in this study was subjected to deep sequencing using ARTIC[51] and found to

542 have a mutation in the furin cleavage site (positions 23606-23608 of NC_045512.2) at a combined

543 frequency of 31%.

544

545 **_Focus forming assay._** Vero E6 cells were seeded at a density of 4×10^4 cells per well in flat-

546 bottom 96-well tissue culture plates. The following day, media was removed and replaced with

547 100 µL of 10-fold serial dilutions of the material to be titered. Two hours later, 135 µL of

548 methylcellulose overlay was added. Plates were incubated for 48 h, then fixed with 4%

549 paraformaldehyde (final concentration) in phosphate-buffered saline for 20 min, followed by

550 permeabilization with saponin-containing buffer. Plates were incubated overnight at 4°C in 100

551 µL of permeabilization buffer containing 1 µg/mL of the CR3022 anti-spike monoclonal antibody[52].

552 Following washing, 50 µL of goat anti-human secondary antibody conjugated to HRP (Sigma

553 AP504P), diluted 1:1000 in permeabilization buffer, was added for 2 hours at room temperature

554   with shaking. Foci were stained with 50 µL of KPL Trueblue (SeraCare), then scanned and

555   automatically quantitated on a Biospot plate reader (Cellular Technology Limited).

556

557   ***Quantitative RT-PCR.*** RNA was extracted using the MagMax mirVana Total RNA isolation kit

558   (Thermo Scientific) on the Kingfisher Flex extraction robot (Thermo Scientific). RNA was reverse

559   transcribed and amplified using the TaqMan RNA-to-CT 1-Step Kit (ThermoFisher). Reverse

560   transcription was carried out at 48°C for 15 min followed by 2 min at 95°C. Amplification was

561   accomplished over 50 cycles as follows: 95°C for 15 s and 60°C for 1 min. Copies of SARS-CoV-

562   2 N gene RNA in samples were determined using a previously published assay[53]. Briefly, a

563   TaqMan assay was designed to target a highly conserved region of the N gene (Forward primer:

564   ATGCTGCAATCGTGCTACAA; Reverse primer: GACTGCCGCCTCTGCTC; Probe: /56-

565   FAM/TCAAGGAAC/ZEN/AACATTGCCAA/3IABkFQ/). This region was included in an RNA

566   standard to allow for copy number determination down to 10 copies per reaction. The reaction

567   mixture contained final concentrations of primers and probe of 500 and 100 nM, respectively. For

568   host genes (ACE2, TMPRSS2, OAS1, MX1, TNF), RNA was reverse-transcribed using the High

569   Capacity cDNA Reverse Transcription Kit (ThermoFisher) and amplified using SYBR Green

570   system (ThermoFisher) with beta2 microglobulin as an internal reference gene.

571

572   ***Quantification of ACE2 expression in RNA-Seq.*** We performed a differential gene expression

573   analysis using R package DESeq2[54] on the Care4DCM cohort[55]. The DESeq2 package utilizes

574   negative binominal distribution to model the distribution of RNA-Seq reads, and uses Wald test to

575   calculate p-values[54]. The Care4DCM cohort included 60 DCM patients and 35 controls[55]. Of the

576   60 DCM patients, 52 received ACEI and 8 received ARB. The myocardial biopsies were extracted

577   from the LV apex by heart catheterization and preserved in liquid nitrogen following standardized

578   protocols. The RNA was extracted from the cardiac tissues using Allprep Kits (Qiagen,

23

579   Düsseldorf, Germany), then the RNA sequencing was carried out using the TrueSeq RNA Sample

580   Prep Kit (Illumina, San Diego, California, USA)[55].

581

582   ***Human atrial tissue samples.*** The study protocol involving human tissue samples was approved

583   by the ethics committees of the Medical Faculty of Heidelberg University (Germany; S-017/2013).

584   Written informed consent was obtained from all patients and the study was conducted in

585   accordance with the Declaration of Helsinki. Tissue samples of right atrial appendages (RAA)

586   were obtained from patients undergoing open heart surgery for coronary artery bypass grafting

587   or valve repair /replacement in the local heart surgery department.

588

589   ***Atrial and ventricular cardiomyocyte isolation.*** After excision, tissue samples were

590   immediately placed into preoxygenated transport solution (100 mM NaCl, 10 mM KCl, 1.2 mM

591   KH2PO4, 5 mM MgSO4, 50 mM taurine, 5 mM 3-[N-morpholino] propane sulfonic acid [MOPS],

592   30 mM 2,3-butanedione monoxime and 20 mM glucose, pH 7.0 with NaOH) and subjected to

593   cardiomyocyte isolation within 15 minutes. RAA tissue samples were dissected into small pieces

594   and rinsed 3 times in Ca2+-free Tyrode's solution (100 mM NaCl, 10 mM KCl, 1.2 mM KH2PO4,

595   5 mM MgSO4, 50 mM taurine, 5 mM 3-(N-morpholino) propane sulfonic acid (MOPS), and 20 mM

596   glucose, pH 7.0 with NaOH) supplemented with 2,3-butanedione monoxime (30 mM BDM; Sigma-

597   Aldrich, St. Louis, MO, USA). The solutions were oxygenated with 100 % O2 at 37°C. After

598   digestion with collagenase type I (288 U/ml; Worthington) and protease type XXIV (5 mg/ml;

599   Sigma-Aldrich) for 15 min and agitation in protease-free solution for another 35 min, the cell

600   suspension was filtered through a 200 nm mesh. Subsequently the Ca2+ concentration of the cell

601   fraction was increased to 0.2 mM, the cell suspension was centrifuged and calcium tolerant rod-

602   shaped single cardiomyocytes were declared as the cardiomyocyte fraction (CM). Remaining

603   tissue chunks were declared as the non cardiomyocyte (NM) fraction. Cells were stored in TRIzol-

604   Reagent (ThermoFisher) at -20°C. Isolation of total RNA was performed, using TRIzol-Reagent

24

605 (ThermoFisher) and frozen tissue samples were processed according to the manufacturer's

606 protocol. Synthesis of single-stranded cDNA was carried out with the Maxima First Strand cDNA

607 Synthesis Kit (ThermoFisher), using 3 µg of total RNA per 20 µl reaction. For quantitative real-

608 time PCR (qPCR) 10 µl reactions, consisting of 0.5 µl cDNA, 5 µl TaqMan Fast Universal Master

609 Mix (ThermoFisher), and 0.5 µl 6-carboxyfluorescein (FAM)-labeled TaqMan probes and primers

610 (TaqMan Gene Expression Assays; ThermoFisher) were analyzed using the StepOnePlus

611 (Applied Biosystems, Foster City, CA, USA) PCR system. hACE2 primers and probes

612 (Hs01085333_m1) were purchased from ThermoFisher. The glyceraldehyde 3-phosphate

613 dehydrogenase housekeeping gene (GAPDH: Hs99999905_m1) was used for normalization. All

614 RT-qPCR reactions were performed as triplicates and control experiments in the absence of

615 cDNA were included. Means of triplicates were used for the $2^{-\Delta Ct}$ calculation, where $2^{-\Delta Ct}$

616 corresponds to the ratio of mRNA expression versus GAPDH.

617

618 ***Flow cytometry.*** Cells were dissociated to single-cell suspension with 0.25% trypsin (Gibco),

619 then washed and incubated with Zombie-violet viability stain (Biolegend) at a dilution of 1:500 in

620 100 µL of PBS at room temperature. In some assays, antibodies against surface proteins were

621 incubated with the cells. Fibroblasts were identified using anti-CD90 PE (Biolegend, catalog

622 number 328110) and macrophages were identified using anti-CD14 APC (Biolegend, catalog

623 number 367118). Cells then were fixed with 4% paraformaldehyde (final concentration) in

624 phosphate-buffered saline for 20 min and analyzed on the MACSQuant 10 (Miltenyi Biotec) or the

625 LSRFortessa X20 (Becton Dickinson Biosciences). Analysis was performed using FlowJo 10.6.1

626 (Becton Dickinson & Co).

627

628 ***hPSC culture and cardiomyocyte differentiation.*** The parent stem cell line, BJFF.6, was

629 generated from the human BJ fibroblast line (ATCC, catalog number: CRL-2522) by the Genome

630 Engineering and iPSC Center at Washington University in St. Louis. This parent cell line has no

631   known mutations associated with heart disease and the stem cells are pluripotent as assessed

632   by immunofluorescence staining[56]. Differentiation to hPSC-derived CMs was performed as

633   previously described [56]. Briefly, stem cells were maintained in feeder-free culture and

634   differentiation was initiated by temporal manipulation of WNT signaling[57,58]. hPSC-derived CMs

635   were enriched using metabolic selection [59], yielding >90% cardiomyocytes [56]. All experiments

636   were conducted at least 30 days after the initiation of differentiation.

637

638   ***Differentiation (and validation) of stem cell derived cardiac fibroblasts.*** hPSC derived

639   cardiac fibroblasts were differentiated using the method of Zhang et al. (reference [45]). Briefly,

640   differentiation was initiated by directing the BJFF stem cell line towards a mesoderm/cardiac

641   progenitor lineage by the activation and subsequent inhibition of WNT signaling using CHIR-

642   99021 and IWP2 respectively. These cells were then directed to become proepicardial cells by

643   the addition of retinoic acid and WNT CHIR 99021 followed by TGFβ inhibition (SB431542, Tocris

644   Bioscience 1614). Finally, the pro-epicardial cells were directed to become quiescent cardiac

645   fibroblasts by the addition of FGF2 and higher levels of TGFβ inhibition. Derivation of hPSC-

646   cardiac fibroblasts was validated by measuring gene expression using RT-PCR. They showed

647   high levels of both cardiac specific genes, GATA4 and TCF21 as well as general fibroblast genes

648   COL1A1 and DDR2 (Fig. S1c).

649

650   ***Fibroblast culture.*** BJ fibroblasts (ATCC, catalog number: CRL-2522) were cultured in Eagle's

651   Minimum Essential Medium with 10% FBS and 1% Pen-Strep (Gibco, catalog number:

652   15140122). Human ventricular cardiac fibroblasts that were harvested from normal adult

653   ventricular tissue were obtained from Lonza, maintained at low passage number (<12), and

654   cultured according to the manufacturer's recommendations in FGM-3 growth media.

655

26

656 ***Macrophage culture.*** CD34$^+$ cells isolated from human cord blood were cultured in Iscove's

657 Modified Dulbecco's Medium with 10% FBS, 1% Pen-Strep, and 10 ng/mL of human macrophage

658 colony stimulating factor (M-CSF, R&D Systems, catalog number 216-MC) for at least 10 days to

659 generate mature macrophages before use in experiments.

660

661 ***Endothelial cell culture.*** H1 hPSCs were differentiated into vascular endothelial cells following

662 the published protocol [60]. Arterial endothelium was identified as CD34+CD184+CD73+ cells using

663 appropriate antibodies (BD Biosciences, anti-CD34 PE-Cy7 [cat # 560710], anti-CD184 APC [cat

664 #560936], anti-CD73 PE [cat #550257]) and isolated by flow cytometric cell sorting on a BD

665 FACSAriaII. These cells were cultured in StemPro-34 serum free media (ThermoFisher, cat#

666 10639011).

667

668 ***Isolation of primary human cardiac endothelial cells and macrophages.*** Human myocardium

669 was dissected into ~200mg pieces and digested in 3mL DMEM containing 250U/mL collagenase

670 IV, 60U/mL hyaluronidase and 60U/mL DNAseI for 45 minutes at 37 degrees C. Following digest

671 and red blood cell lysis, the resultant single cell suspension was incubated with anti-CD14 PE

672 (cat #301806), anti-CD64 PE-Cy7 (cat #305022), anti-CD45 FITC (cat #304006), and anti-CD31

673 BV421 (cat #303124) (all antibodies from Biolegend). Macrophages were identified as

674 CD14+CD64+CD45+ cells and endothelial cells were identified as CD31+CD64-CD45- cells.

675 Cells were isolated by flow cytometric cell sorting on a BD FACSMelody and cultured in StemPro-

676 34 supplemented with either M-CSF or VEGF (R&D Systems, cat #293-VE).

677

678 ***Two-dimensional cell cultures and tissues.*** hPSC-derived CMs, fibroblasts, and/or

679 macrophages were dissociated from two-dimensional cultures using 0.25% Trypsin-EDTA,

680 resuspended in media containing RPMI-1640 with 20% FBS and 10 µM Y-27632 and plated on

681 gelatin coated tissue culture dishes. After 48 h, the media was changed to DMEM High glucose

27

682 (4 mg/mL), 10% FBS, 1% non-essential amino acids, 1% GlutaMAX Supplement, and 1% Pen-

683 Strep. All drug compounds were purchased from Selleckchem (ruxolitinib, catalog number S8932;

684 MRT67307, catalog number S7948; E64, catalog number S7379; camostat, catalog number

685 S2874) and resuspended to a stock concentration of 10μM in PBS or DMSO (depending on the

686 solubility profile), then diluted to working concentration in culture media (described above) and

687 sterile-filtered.

688

689 ***Immunostaining of hPSC-derived CMs and confocal fluorescence microscopy.***

690 Immunostaining was performed as previously described with a few modifications[56]. Briefly,

691 cardiomyocytes were fixed for 20 minutes in 4% formaldehyde in phosphate buffered saline

692 (PBS). Cells were then permeabilized with 0.4% Triton X-100 for 20 minutes at room temperature.

693 The cells were blocked for 1 hour using a blocking solution containing 3% bovine serum albumin,

694 5% donkey serum, 0.1% Triton X-100, and 0.02% sodium azide in PBS. Primary antibodies (rabbit

695 anti Troponin T, 1:400, Abcam, ab45932) were added for 1-2 hours at room temperature or

696 overnight at 4 °C. Cells were then washed with PBS before incubating for 1 hour in secondary

697 antibody (Cy3 donkey anti-rabbit, Jackson Immunoresearch, 711165152). 4′,6-diamidino-2-

698 phenylindole (DAPI) was used at a 1:50000 dilution to stain for nuclei. Cells were visualized using

699 a Nikon A1Rsi confocal microscope (Washington University Center for Cellular Imaging). Z-

700 stacks of cells with 40x magnification were recorded in sequential scanning mode. Images were

701 processed in ImageJ and Z-stacks were converted to standard deviation projections[61].

702

703 ***Engineered heart tissues (EHTs).*** EHTs were prepared according to published protocol[62] with

704 modifications. Casting molds for tissue formation were prepared using PDMS at a 1:25 ratio. 1

705 mL of PDMS was poured into each well of a 24-well plate and a Teflon spacer (EHT Technologies

706 GmBH; Hamburg, Germany) was placed inside to generate a well. The PDMS was degassed

707   under high vacuum and baked overnight at 65°C. The Teflon spacers were removed using

708   ethanol.

709   Prior to use, the casting molds were sterilized with ethanol, dried with nitrogen gas, and placed

710   under UV light for 10-15 min. 1% pluronic-F127 in PBS was added to the molds for 20 min to

711   block the surface from adhering to the seeded tissues. The pluronic was removed, the casting

712   molds were rinsed twice with PBS, and then dried. Silicone racks consisting of two pairs of PDMS

713   posts (EHT Technologies GmBH, Hamburg, Germany) were positioned such that each pair of

714   PDMS posts fit within one casting mold.

715   The procedure for seeding of tissues was modified from[62]. Working on ice, rat collagen I (1 mg/mL

716   final concentration) was combined with equal parts 2x DMEM containing FBS and neutralized

717   with sodium hydroxide. Growth factor reduced Matrigel (Corning, catalog number: 354230) was

718   added to a final concentration of 0.77 g/mL. hPSC-derived CMs, fibroblasts, and/or macrophages

719   were dissociated from two-dimensional cultures with 0.25% Trypsin-EDTA and the Trypsin was

720   quenched in RPMI-1640 with 20% FBS media containing 10 g/mL of DNaseI. Cells were then

721   centrifuged, resuspended in media containing RPMI-1640 with 20% FBS and 10 μM Y-27632,

722   and combined with the collagen/Matrigel mixture. Each tissue contained 10^6 hPSC-derived CMs,

723   5% fibroblasts, and 10% macrophages. Tissues were seeded in the casting molds with the

724   silicone racks in a 100 μL volume. After polymerizing around the silicone racks for 2 h at 37°C,

725   the tissues were covered overnight with RPMI-1640 containing 20% FBS. The tissues, attached

726   to the posts of the silicone racks, then were moved out of the casting molds and transferred into

727   media containing DMEM High glucose (4 mg/mL), 10% FBS, 1% non-essential amino acids, 1%

728   GlutaMAX Supplement, and 1% Pen-Strep. Consistent with previous reports, engineered heart

729   tissue contraction was observed ~2-5 days after seeding, and the displacement increased over

730   time as the tissues organize and mature[62]. By day 7 post seeding, all tissues generated aey t

731   least 0.025 mm of displacement (see details below). EHTs were inoculated with SARS-CoV-2 at

732   least 7 days after tissue seeding, and EHT contraction and morphology were measured daily

733   throughout the course of the experiment.

734

735   ***Analysis of engineered heart tissue contractility.*** EHTs between two PDMS posts were

736   visualized on an EVOS microscope and videos of spontaneously contracting posts were recorded

737   at 30 frames per second using a Macintosh desktop with built-in camera (**Supplementary Videos**

738   **1 and 2**). We used the 2 mm diameter of the caps on the posts to calibrate the pixels per mm for

739   each video. We wrote a custom script in MATLAB to calculate the displacement of the posts as a

740   function of time. Automated tracking was done using the computer vision toolbox and the

741   displacement was calculated as a function of time. A second order polynomial spline fit was

742   applied to remove any drift in the camera position. Traces were smoothed using a Savitsky-Golay

743   filter and peaks in the displacement were identified using the findpeaks algorithm. The average

744   and standard deviation of the displacement was then calculated for each ~60 sec video. The time

745   for force development was defined as the time required to achieve 75% activation and the time

746   for relaxation was defined as the time to relax to 75% of the peak activation.

747

748   ***Histology of autopsy and engineered heart tissues.*** Tissues were fixed with 10% NBF for 7

749   days, embedded in 1% agar, mounted in cassettes, and embedded in paraffin. Target markers

750   were visualized using Opal 4-Color Manual IHC Kit (Perkin-Elmer) with the following changes: 1)

751   10% NBF fixation step was substituted for treatment with 10% MeOH + 10% hydrogen peroxide

752   in water for 20 min; 2) during antigen retrieval, the vessel with AR6 was brought to boiling and

753   slides were immediately transferred into deionized water; 3) blocking buffer was substituted for

754   10% FBS in TBST. Primary antibodies against human sarcomeric actin (Sigma A2127), human

755   Troponin T (ThermoFisher MS-295-P1), human CD68 (BioRad MCA5709), human ACE2 (Abcam

756   ab15348), human Ki67 (Abcam ab16667), human CCR2 (Abcam ab176390), SARS-CoV-2-N

30

757   (Sino Biological 40143-R001) were used. Cell death was assessed using TUNEL staining from *In*

758   *Situ* Cell Death Detection Kit (Roche) with Opal-based costain for sarcomeric actin as described

759   above. Viral RNA was directly visualized with RNAscope Multiplex Fluorescent Reagent Kit v2

760   Assay (Advanced Cell Diagnostics) and RNAscope 2.5 HD Detection Reagent - RED (Advanced

761   Cell Diagnostics) using positive-strand and negative strand probes for ORF1ab. Images were

762   collected on a confocal microscope (Zeiss LSM 700 Laser Scanning Confocal) and processed

763   using ZenBlack (Zeiss) and ImageJ (NCBI). Troponin staining was quantified using manual cell

764   tracing in ImageJ (NCBI) from at least three areas and 30 cells analyzed per tissue.

765

766   ***Electron microscopy.*** Cells grown on aclar coverslips were briefly rinsed in 0.15 M cacodylate

767   buffer that was warmed to 37˚C followed by the addition of 2.5% glutaraldehyde, 2%

768   paraformaldehyde, 0.2% tannic acid in 0.15 M cacodylate buffer with 2 mM $CaCl_2$, pH 7.4 at 37˚C.

769   Once added, the coverslips were returned to a 37˚C incubator for 15 min followed by overnight

770   fixation at room temperature. Post fixation, samples were rinsed in 0.15 M cacodylate buffer 4

771   times for 15 min each followed by a secondary fixation in 1% OsO_4/1.5% $K_3Fe(CN)_6$ in 0.15 M

772   cacodylate buffer for 1.5 h in the dark. The coverslips were then rinsed 4 times in ultrapure water

773   for 15 min each followed by *en bloc* staining with 2% aqueous uranyl acetate overnight at 4˚C in

774   the dark. After another 4 water washes, the samples were dehydrated in a graded ethanol series

775   (30%, 50%, 70%, 90%, 100% x4) for 10 min for each step. Once dehydrated, cells were infiltrated

776   with LX112 resin over a period of 2 days. The coverslips then were flat embedded and

777   polymerized at 60˚C for 48 h. Once polymerized, the aclar coverslips were peeled away from the

778   resin, and small areas were excised and mounted perpendicularly on a blank epoxy stub for cross

779   sectioning. 70 nm sections were then cut and imaged on a TEM (JEOL JEM-1400 Plus) at 120

780   KeV.

781

782 ***RNA sequencing and analysis.*** Samples were prepared according to library kit manufacturer's

783 protocol, indexed, pooled, and sequenced on an Illumina NovaSeq 6000. Basecalls and

784 demultiplexing were performed with Illumina's bcl2fastq software and a custom python

785 demultiplexing program with a maximum of one mismatch in the indexing read. RNA-seq reads

786 were then aligned to the Human Ensembl GRCh38.76 primary assembly and SARS-CoV-2 NCBI

787 NC_045512 Wuhan-Hu-1 genome with STAR version 2.5.1a[63]. Gene counts were derived from

788 the number of uniquely aligned unambiguous reads by Subread:featureCount version 1.4.6-p5[64].

789 Isoform expression of known Ensembl transcripts were estimated with Salmon version 0.8.2[65].

790 Sequencing performance was assessed for the total number of aligned reads, total number of

791 uniquely aligned reads, and features detected. The ribosomal fraction, known junction saturation,

792 and read distribution over known gene models were quantified with RSeQC version 2.6.2[66].

793 All gene counts were imported into the R/Bioconductor package EdgeR[67] and TMM normalization

794 size factors were calculated to adjust for samples for differences in library size. Ribosomal genes

795 and genes not expressed in at least four samples greater than one count-per-million were

796 excluded from further analysis. The TMM size factors and the matrix of counts were then imported

797 into the R/Bioconductor package Limma[68]. Weighted likelihoods based on the observed mean-

798 variance relationship of every gene and sample were then calculated for all samples with the

799 voomWithQualityWeights[69]. The performance of all genes was assessed with plots of the residual

800 standard deviation of every gene to their average log-count with a robustly fitted trend line of the

801 residuals. Differential expression analysis was then performed to analyze for differences between

802 conditions and the results were filtered for only those genes with Benjamini-Hochberg false-

803 discovery rate adjusted p-values less than or equal to 0.05.

804 For each contrast extracted with Limma, global perturbations in known Gene Ontology (GO)

805 terms, MSigDb, and KEGG pathways were detected using the R/Bioconductor package GAGE[70]

806 to test for changes in expression of the reported log 2 fold-changes reported by Limma in each

32

807 term versus the background log 2 fold-changes of all genes found outside the respective term.

808 The R/Bioconductor package heatmap3[71] was used to display heatmaps across groups of

809 samples for each GO or MSigDb term with a Benjamini-Hochberg false-discovery rate adjusted

810 p-value less than or equal to 0.05. Perturbed KEGG pathways where the observed log 2 fold-

811 changes of genes within the term were significantly perturbed in a single-direction versus

812 background or in any direction compared to other genes within a given term with p-values less

813 than or equal to 0.05 were rendered as nnotated KEGG graphs with the R/Bioconductor package

814 Pathview[72].

815 To find the most critical genes, the raw counts were variance stabilized with the R/Bioconductor

816 package DESeq2[54] and then analyzed via weighted gene correlation network analysis with the

817 R/Bioconductor package WGCNA[73]. Briefly, all genes were correlated across each other by

818 Pearson correlations and clustered by expression similarity into unsigned modules using a power

819 threshold empirically determined from the data. An eigengene was created for each de novo

820 cluster and its expression profile was then correlated across all coefficients of the model matrix.

821 Because these clusters of genes were created by expression profile rather than known functional

822 similarity, the clustered modules were given the names of random colors where grey is the only

823 module that has any pre-existing definition of containing genes that do not cluster well with others.

824 These *de novo* clustered genes were then tested for functional enrichment of known GO terms

825 with hypergeometric tests available in the R/Bioconductor package clusterProfiler[74]. Significant

826 terms with Benjamini-Hochberg adjusted p-values less than 0.05 were then collapsed by similarity

827 into clusterProfiler category network plots to display the most significant terms for each module

828 of hub genes in order to interpolate the function of each significant module. The information for

829 all clustered genes for each module were combined with their respective statistical significance

830 results from Limma to identify differentially expressed genes.

831

832   **Statistical analysis.** Statistical tests were chosen based on standards in the virology and

833   cardiomyocyte fields for given assay. Parametric and non-parametric statistical methods were

834   used when appropriate. Statistical significance was assigned when P values were < 0.05 using

835   Prism Version 8 (GraphPad). Specific tests are indicated in the figure legends.

836   **Data availability**. All data supporting the findings of this study are found within the paper and its

837   Extended Data Figures and are available from the corresponding authors upon request. RNA

838   sequencing data sets generated in this study will be made available in GEO at the time of

839   publication.

854

Conflicts of interest/Competing interests:

856 Kory Lavine - Medtronic: DT-PAS/APOGEE trial advisory board. M.S.D. is a consultant for Inbios,

857 Eli Lilly, Vir Biotechnology, NGM Biopharmaceuticals, and on the Scientific Advisory Board of

858 Moderna. The Lavine laboratory has received funding and unrelated sponsored research

859 agreements from Amgen. The Diamond laboratory has received funding and unrelated sponsored

860 research agreements from Moderna, Vir Biotechnology, and Emergent BioSolutions. Lina

861 Greenberg, W. Tom Stump, Michael Greenberg, Adam Bailey, Oleksandr Dmytrenko, Andrea

862 Bredemeyer - None.

863

864

865 **Author Contributions:**

866 Conceptualization, M.J.G, A.L.Bailey, K.L, M.S.D.; Methodology, L.G., W.T.S., A.L.Bailey;

867 Software, M.J.G.; Investigation, L.G., O.D., A.L.Bailey, A.L.Bredemeyer, P.M., J.L., V.P., E.W.,

868 S.S, J.A.F., W.G., C.S.; Resources, E.B., A.J.N, K.A.H., A.S.R, M.S., D.H., X.X., P-Y.S, J.T.H,

869 F.L., W.T.S., L.S.; Writing – Original Draft, L.G., M.J.G., A.L.Bailey, K.L., O.D., A.L.Bredemeyer;

870 Writing – Review & Editing, L.G., M.J.G., A.L.Bailey, K.L., O.D., A.L.Bredemeyer, M.S.D.; Funding

871 Acquisition, M.J.G, K.L., M.S.D; Supervision, M.S.D., M.J.G, C-Y.L., K.L.

872

References:

1. Madjid, M., Safavi-Naeini, P., Solomon, S. D. & Vardeny, O. Potential Effects of Coronaviruses on the Cardiovascular System: A Review. *JAMA Cardiol.* (2020) doi:10.1001/jamacardio.2020.1286.

2. Zhou, F. *et al.* Clinical course and risk factors for mortality of adult inpatients with COVID-19 in Wuhan, China: a retrospective cohort study. *Lancet Lond. Engl.* **395**, 1054–1062 (2020).

3. Shi, S. *et al.* Association of Cardiac Injury With Mortality in Hospitalized Patients With COVID-19 in Wuhan, China. *JAMA Cardiol.* (2020) doi:10.1001/jamacardio.2020.0950.

4. Bhatla, A. *et al.* COVID-19 and Cardiac Arrhythmias. *Heart Rhythm* (2020) doi:10.1016/j.hrthm.2020.06.016.

5. Huang, L. *et al.* Cardiac Involvement in Patients Recovered From COVID-2019 Identified Using Magnetic Resonance Imaging. *JACC Cardiovasc. Imaging* (2020) doi:10.1016/j.jcmg.2020.05.004.

6. Puntmann, V. O. *et al.* Outcomes of Cardiovascular Magnetic Resonance Imaging in Patients Recently Recovered From Coronavirus Disease 2019 (COVID-19). *JAMA Cardiol.* (2020) doi:10.1001/jamacardio.2020.3557.

7. Rajpal, S. *et al.* Cardiovascular Magnetic Resonance Findings in Competitive Athletes Recovering From COVID-19 Infection. *JAMA Cardiol.* (2020) doi:10.1001/jamacardio.2020.4916.

8. Tersalvi, G. *et al.* Elevated Troponin in Patients With Coronavirus Disease 2019: Possible Mechanisms. *J. Card. Fail.* **26**, 470–475 (2020).

9. Cleary, S. J. *et al.* Animal models of mechanisms of SARS-CoV-2 infection and COVID-19 pathology. *Br. J. Pharmacol.* (2020) doi:10.1111/bph.15143.

10. Letko, M., Marzi, A. & Munster, V. Functional assessment of cell entry and receptor usage for SARS-CoV-2 and other lineage B betacoronaviruses. *Nat. Microbiol.* **5**, 562–569 (2020).

899   11. Wan, Y., Shang, J., Graham, R., Baric, R. S. & Li, F. Receptor Recognition by the Novel

900   Coronavirus from Wuhan: an Analysis Based on Decade-Long Structural Studies of SARS

901   Coronavirus. *J. Virol.* **94**, (2020).

902   12. Greenberg, M. J., Daily, N. J., Wang, A., Conway, M. K. & Wakatsuki, T. Genetic and Tissue

903   Engineering Approaches to Modeling the Mechanics of Human Heart Failure for Drug

904   Discovery. *Front. Cardiovasc. Med.* **5**, 120 (2018).

905   13. Weinberger, F., Mannhardt, I. & Eschenhagen, T. Engineering Cardiac Muscle Tissue: A

906   Maturating Field of Research. *Circ. Res.* **120**, 1487–1500 (2017).

907   14. Karbassi, E. *et al.* Cardiomyocyte maturation: advances in knowledge and implications for

908   regenerative medicine. *Nat. Rev. Cardiol.* **17**, 341–359 (2020).

909   15. Hoffmann, M. *et al.* SARS-CoV-2 Cell Entry Depends on ACE2 and TMPRSS2 and Is

910   Blocked by a Clinically Proven Protease Inhibitor. *Cell* **181**, 271-280.e8 (2020).

911   16. Bao, L. *et al.* The pathogenicity of SARS-CoV-2 in hACE2 transgenic mice. *Nature* (2020)

912   doi:10.1038/s41586-020-2312-y.

913   17. Chen, L., Li, X., Chen, M., Feng, Y. & Xiong, C. The ACE2 expression in human heart

914   indicates new potential mechanism of heart injury among patients infected with SARS-CoV-

915   2. *Cardiovasc. Res.* **116**, 1097–1100 (2020).

916   18. Xie, X. *et al.* An Infectious cDNA Clone of SARS-CoV-2. *Cell Host Microbe* **27**, 841-848.e3

917   (2020).

918   19. Goldsmith, C. S. *et al.* Ultrastructural characterization of SARS coronavirus. *Emerg. Infect.*

919   *Dis.* **10**, 320–326 (2004).

920   20. Goldsmith, C. S., Miller, S. E., Martines, R. B., Bullock, H. A. & Zaki, S. R. Electron

921   microscopy of SARS-CoV-2: a challenging task. *Lancet Lond. Engl.* **395**, e99 (2020).

922   21. Kim, D. *et al.* The Architecture of SARS-CoV-2 Transcriptome. *Cell* **181**, 914-921.e10

923   (2020).

924   22. Gordon, C. J. *et al.* Remdesivir is a direct-acting antiviral that inhibits RNA-dependent RNA

925   polymerase from severe acute respiratory syndrome coronavirus 2 with high potency. *J.*

926   *Biol. Chem.* **295**, 6785–6797 (2020).

927   23. Yin, W. *et al.* Structural basis for inhibition of the RNA-dependent RNA polymerase from

928   SARS-CoV-2 by remdesivir. *Science* **368**, 1499–1504 (2020).

929   24. Agostini, M. L. *et al.* Coronavirus Susceptibility to the Antiviral Remdesivir (GS-5734) Is

930   Mediated by the Viral Polymerase and the Proofreading Exoribonuclease. *mBio* **9**, (2018).

931   25. Simmons, G., Zmora, P., Gierer, S., Heurich, A. & Pöhlmann, S. Proteolytic activation of the

932   SARS-coronavirus spike protein: cutting enzymes at the cutting edge of antiviral research.

933   *Antiviral Res.* **100**, 605–614 (2013).

934   26. Cooper, L. T. Myocarditis. *N. Engl. J. Med.* **360**, 1526–1538 (2009).

935   27. Leone, O., Pieroni, M., Rapezzi, C. & Olivotto, I. The spectrum of myocarditis: from

936   pathology to the clinics. *Virchows Arch. Int. J. Pathol.* **475**, 279–301 (2019).

937   28. Hu, H., Ma, F., Wei, X. & Fang, Y. Coronavirus fulminant myocarditis saved with

938   glucocorticoid and human immunoglobulin. *Eur. Heart J.* (2020)

939   doi:10.1093/eurheartj/ehaa190.

940   29. Zhou, R., Zhang, Q. & Xu, P. TBK1, a central kinase in innate immune sensing of nucleic

941   acids and beyond. *Acta Biochim. Biophys. Sin.* **52**, 757–767 (2020).

942   30. Bartok, E. & Hartmann, G. Immune Sensing Mechanisms that Discriminate Self from Altered

943   Self and Foreign Nucleic Acids. *Immunity* **53**, 54–77 (2020).

944   31. Michaud, K. *et al.* Diagnosis of myocardial infarction at autopsy: AECVP reappraisal in the

945   light of the current clinical classification. *Virchows Arch. Int. J. Pathol.* **476**, 179–194 (2020).

946   32. Sabatasso, S. *et al.* Early markers for myocardial ischemia and sudden cardiac death. *Int. J.*

947   *Legal Med.* **130**, 1265–1280 (2016).

948   33. Aljakna, A. *et al.* Multiplex quantitative imaging of human myocardial infarction by mass

949   spectrometry-immunohistochemistry. *Int. J. Legal Med.* **132**, 1675–1684 (2018).

950   34. Bojkova, D. *et al.* SARS-CoV-2 infects and induces cytotoxic effects in human

951   cardiomyocytes. *Cardiovasc. Res.* (2020) doi:10.1093/cvr/cvaa267.

952   35. Tavazzi, G. *et al.* Myocardial localization of coronavirus in COVID-19 cardiogenic shock.

953   *Eur. J. Heart Fail.* **22**, 911–915 (2020).

954   36. Puelles, V. G. *et al.* Multiorgan and Renal Tropism of SARS-CoV-2. *N. Engl. J. Med.* (2020)

955   doi:10.1056/NEJMc2011400.

956   37. Lindner, D. *et al.* Association of Cardiac Infection With SARS-CoV-2 in Confirmed COVID-

957   19 Autopsy Cases. *JAMA Cardiol.* (2020) doi:10.1001/jamacardio.2020.3551.

958   38. Lamers, M. M. *et al.* SARS-CoV-2 productively infects human gut enterocytes. *Science*

959   (2020) doi:10.1126/science.abc1669.

960   39. Monteil, V. *et al.* Inhibition of SARS-CoV-2 Infections in Engineered Human Tissues Using

961   Clinical-Grade Soluble Human ACE2. *Cell* **181**, 905-913.e7 (2020).

962   40. Yang, L. *et al.* A Human Pluripotent Stem Cell-based Platform to Study SARS-CoV-2

963   Tropism and Model Virus Infection in Human Cells and Organoids. *Cell Stem Cell* **27**, 125-

964   136.e7 (2020).

965   41. Bos, J. M. *et al.* Marked Up-Regulation of ACE2 in Hearts of Patients With Obstructive

966   Hypertrophic Cardiomyopathy: Implications for SARS-CoV-2-Mediated COVID-19. *Mayo*

967   *Clin. Proc.* **95**, 1354–1368 (2020).

968   42. Crackower, M. A. *et al.* Angiotensin-converting enzyme 2 is an essential regulator of heart

969   function. *Nature* **417**, 822–828 (2002).

970   43. Hinson, J. T. *et al.* HEART DISEASE. Titin mutations in iPS cells define sarcomere

971   insufficiency as a cause of dilated cardiomyopathy. *Science* **349**, 982–986 (2015).

972   44. Wijnker, P. J. M. *et al.* Comparison of the effects of a truncating and a missense MYBPC3

973   mutation on contractile parameters of engineered heart tissue. *J. Mol. Cell. Cardiol.* **97**, 82–

974   92 (2016).

975   45. Zhang, H. *et al.* Generation of Quiescent Cardiac Fibroblasts From Human Induced

976   Pluripotent Stem Cells for In Vitro Modeling of Cardiac Fibrosis. *Circ. Res.* **125**, 552–566

977   (2019).

978   46. Lian, X. *et al.* Efficient differentiation of human pluripotent stem cells to endothelial

979   progenitors via small-molecule activation of WNT signaling. *Stem Cell Rep.* **3**, 804–816

980   (2014).

981   47. Dutsch, A. *et al.* Phosphomimetic cardiac myosin-binding protein C partially rescues a

982   cardiomyopathy phenotype in murine engineered heart tissue. *Sci. Rep.* **9**, 18152 (2019).

983   48. Truitt, R. *et al.* Increased Afterload Augments Sunitinib-Induced Cardiotoxicity in an

984   Engineered Cardiac Microtissue Model. *JACC Basic Transl. Sci.* **3**, 265–276 (2018).

985   49. Zang, R. *et al.* TMPRSS2 and TMPRSS4 promote SARS-CoV-2 infection of human small

986   intestinal enterocytes. *Sci. Immunol.* **5**, (2020).

987   50. Zhou, J. *et al.* Infection of bat and human intestinal organoids by SARS-CoV-2. *Nat. Med.*

988   (2020) doi:10.1038/s41591-020-0912-6.

989   51. Pipelines, D. *et al.* COVID-19 ARTIC v3 Illumina library construction and sequencing

990   protocol v4 (protocols.io.bgxjjxkn). doi:10.17504/protocols.io.bgxjjxkn.

991   52. ter Meulen, J. *et al.* Human monoclonal antibody combination against SARS coronavirus:

992   synergy and coverage of escape mutants. *PLoS Med.* **3**, e237 (2006).

993   53. Case, J. B., Bailey, A. L., Kim, A. S., Chen, R. E. & Diamond, M. S. Growth, detection,

994   quantification, and inactivation of SARS-CoV-2. *Virology* **548**, 39–48 (2020).

995   54. Love, M. I., Huber, W. & Anders, S. Moderated estimation of fold change and dispersion for

996   RNA-seq data with DESeq2. *Genome Biol.* **15**, 550 (2014).

997   55. Meder, B. *et al.* Epigenome-Wide Association Study Identifies Cardiac Gene Patterning and

998   a Novel Class of Biomarkers for Heart Failure. *Circulation* **136**, 1528–1544 (2017).

999   56. Clippinger, S. R. *et al.* Disrupted mechanobiology links the molecular and cellular

1000   phenotypes in familial dilated cardiomyopathy. *Proc. Natl. Acad. Sci. U. S. A.* **116**, 17831–

1001   17840 (2019).

1002   57. Lian, X. *et al.* Robust cardiomyocyte differentiation from human pluripotent stem cells via

1003   temporal modulation of canonical Wnt signaling. *Proc. Natl. Acad. Sci. U. S. A.* **109**, E1848-

1004   1857 (2012).

1005   58. Lian, X. *et al.* Directed cardiomyocyte differentiation from human pluripotent stem cells by

1006   modulating Wnt/β-catenin signaling under fully defined conditions. *Nat. Protoc.* **8**, 162–175

1007   (2013).

1008   59. Sharma, A. *et al.* Derivation of highly purified cardiomyocytes from human induced

1009   pluripotent stem cells using small molecule-modulated differentiation and subsequent

1010   glucose starvation. *J. Vis. Exp. JoVE* (2015) doi:10.3791/52628.

1011   60. Dege, C. & Sturgeon, C. M. Directed Differentiation of Primitive and Definitive

1012   Hematopoietic Progenitors from Human Pluripotent Stem Cells. *J. Vis. Exp. JoVE* (2017)

1013   doi:10.3791/55196.

1014   61. Schindelin, J. *et al.* Fiji: an open-source platform for biological-image analysis. *Nat. Methods*

1015   **9**, 676–682 (2012).

1016   62. Breckwoldt, K. *et al.* Differentiation of cardiomyocytes and generation of human engineered

1017   heart tissue. *Nat. Protoc.* **12**, 1177–1197 (2017).

1018   63. Dobin, A. *et al.* STAR: ultrafast universal RNA-seq aligner. *Bioinforma. Oxf. Engl.* **29**, 15–21

1019   (2013).

1020   64. Liao, Y., Smyth, G. K. & Shi, W. featureCounts: an efficient general purpose program for

1021   assigning sequence reads to genomic features. *Bioinforma. Oxf. Engl.* **30**, 923–930 (2014).

1022   65. Patro, R., Duggal, G., Love, M. I., Irizarry, R. A. & Kingsford, C. Salmon provides fast and

1023   bias-aware quantification of transcript expression. *Nat. Methods* **14**, 417–419 (2017).

1024   66. Wang, L., Wang, S. & Li, W. RSeQC: quality control of RNA-seq experiments. *Bioinforma.*

1025   *Oxf. Engl.* **28**, 2184–2185 (2012).

1026   67. Robinson, M. D., McCarthy, D. J. & Smyth, G. K. edgeR: a Bioconductor package for

1027   differential expression analysis of digital gene expression data. *Bioinforma. Oxf. Engl.* **26**,

1028   139–140 (2010).

1029   68. Ritchie, M. E. *et al.* limma powers differential expression analyses for RNA-sequencing and

1030   microarray studies. *Nucleic Acids Res.* **43**, e47 (2015).

1031   69. Liu, R. *et al.* Why weight? Modelling sample and observational level variability improves

1032   power in RNA-seq analyses. *Nucleic Acids Res.* **43**, e97 (2015).

1033   70. Luo, W., Friedman, M. S., Shedden, K., Hankenson, K. D. & Woolf, P. J. GAGE: generally

1034   applicable gene set enrichment for pathway analysis. *BMC Bioinformatics* **10**, 161 (2009).

1035   71. Zhao, S., Guo, Y., Sheng, Q. & Shyr, Y. Advanced heat map and clustering analysis using

1036   heatmap3. *BioMed Res. Int.* **2014**, 986048 (2014).

1037   72. Luo, W. & Brouwer, C. Pathview: an R/Bioconductor package for pathway-based data

1038   integration and visualization. *Bioinforma. Oxf. Engl.* **29**, 1830–1831 (2013).

1039   73. Langfelder, P. & Horvath, S. WGCNA: an R package for weighted correlation network

1040   analysis. *BMC Bioinformatics* **9**, 559 (2008).

1041   74. Yu, G., Wang, L.-G., Han, Y. & He, Q.-Y. clusterProfiler: an R package for comparing

1042   biological themes among gene clusters. *Omics J. Integr. Biol.* **16**, 284–287 (2012).

1043
1044

1045 **Key Resources Table:**

REAGENT or RESOURCE	SOURCE	IDENTIFIER
Antibodies		
Anti-CoV spike	PMID: 16796401	CR3022
Anti-human CD14 APC	Biolegend	RRID: AB_314190
Anti-human CD68	BioRad	RRID: AB_2074721
Anti-human Sarcomeric actin	Sigma	Clone: A2127
Anti-human ACE2	Abcam	RRID: AB_301861
Anti-human Ki67	Abcam	RRID: AB_302459
Anti-SARS-CoV-2 nucleocaspid protein	Sino Biological	RRID: AB_2827974
Anti-TNNT2	Miltenyi Biotech	RRID: AB_2783891
Anti-human CCR2	Abcam	Cat# ab176390
Anti-rabbit TNNT2	Abcam	Cat# ab45932
Cy3 donkey anti-rabbit	Jackson Immunoresearch	Cat# 711165152
Anti-human TNNT2	ThermoFisher	Cat# MS-295-P0
Anti-human CD14 PE	Biolegend	RRID: AB_314188
Anti-human CD64 PE-Cy7	Biolegend	RRID: AB_2561584
Anti-human CD45 FITC	Biolegend	RRID: AB_314394
Anti-human CD31 BV421	Biolegend	RRID: AB_2563810

Anti-human CD90 PE	Biolegend	RRID: AB_893433
Anti-human CD34 PE-Cy7	BD Biosciences	Cat # 560710
Anti-human CD184 APC	BD Biosciences	Cat #560936
Anti-human CD73 PE	BD Biosciences	Cat #550257
Bacterial and Virus Strains		
SARS-CoV-2	CDC	2019n-CoV/USA_WA1/2019
SARS-CoV-2_mNeonGreen	PY Shi	PMID: 32289263
Chemicals, Peptides, and Recombinant Proteins		
Camostat Mesilate	Selleckchem	S2874
E-64	Selleckchem	S7379
Remdesivir		
SB431542	Tocris	1614
M-CSF	R&D Systems	Cat # 216-MC
VEGF	R&D Systems	Cat # 293-VE
Critical Commercial Assays		
Opal 4-Color Manual IHC Kit	Perkin-Elmer	Cat# NEL810001KT
In Situ Cell Death Detection Kit	Roche	Cat# 12156792910

RNAscope 2.5 HD Detection Reagent – RED	Advanced Cell Diagnostics	Cat# 322360
RNAscope Multiplex Fluorescent Reagent Kit v2 Assay	Advanced Cell Diagnostics	Cat# 323100
Experimental Models: Cell Lines		
human BJ fibroblast cells	ATCC	Cat#CRL-2522
human induced pluripotent stem cell line	Genome Engineering and iPSC Center at Washington University	Cat#BJFF.6
Experimental Models: Organisms/Strains		
Oligonucleotides		
F: ATGCTGCAATCGTGCTACAA	IDT	PMC7293183
R: GACTGCCGCCTCTGCTC	IDT	PMC7293183
P: 56-FAM/TCAAGGAAC/ZEN/AACATTGCCAA/3IABkFQ/	IDT	PMC7293183
Primers for B2M, ACE2, TMPRSS2, MYH7, TNNT2, OAS1, MX1 in table S1	IDT	N/A
Software and Algorithms		
MATLAB	Mathworks	Version 2020a
Other		
Dow SYLGARD™ 184 Silicone Encapsulant Clear 0.5 kg Kit	Ellsworth Adhesives	Cat#184 SIL ELAST KIT 0.5KG
Collagen I, Rat Tail	Corning	Cat#354236

Y-27632	Selleck Chemicals	Cat#S1049
Teflon spacer	EHT Technologies GmBH	Cat#C0002
Silicone rack	EHT Technologies GmBH	Cat#C0001
Pluronic F-127	ThermoFisher	Cat#P6866
Growth Factor Reduced Matrigel	Corning	Cat#354230
Fetal bovine serum (FBS)	MilliporeSigma	Cat#F0926

1046

1047

1048

1049

1050

1051

1052

1053   Table S1. Primers for qPCR-base evaluation of human host gene expression

Gene	Forward (5'-3')	Reverse (5'-3')
ACE2	GAGAAGTGGAGGTGGATGG	ACATGGAACAGAGATGCGG
TMPRSS2	GGAGTGTACGGGAATGTGATG	CCAGCCCCATTGTTTTCTTG
B2M	TGCTGTCTCCATGTTTGATGTATCT	TCTCTGCTCCCCACCTCTAAGT
TNNT2	AGCGGAAAAGTGGGAAGAG	TCCAAGTTATAGATGCTCTGCC
Oas1	CATCTGTGGGTTCCTGAAGG	GAGAGGACTGAGGAAGACAAC
Mx1	GAAGATAAGTGGAGAGGCAAGG	CTCCAGGGTGATTAGCTCATG
TNF	ACTTTGGAGTGATCGGCC	GCTTGAGGGTTTGCTACAAC
MYH7	CATTGACTTTGGCATGGACC	CAAACAGCTTGGCCTTGAAG

1054

1055
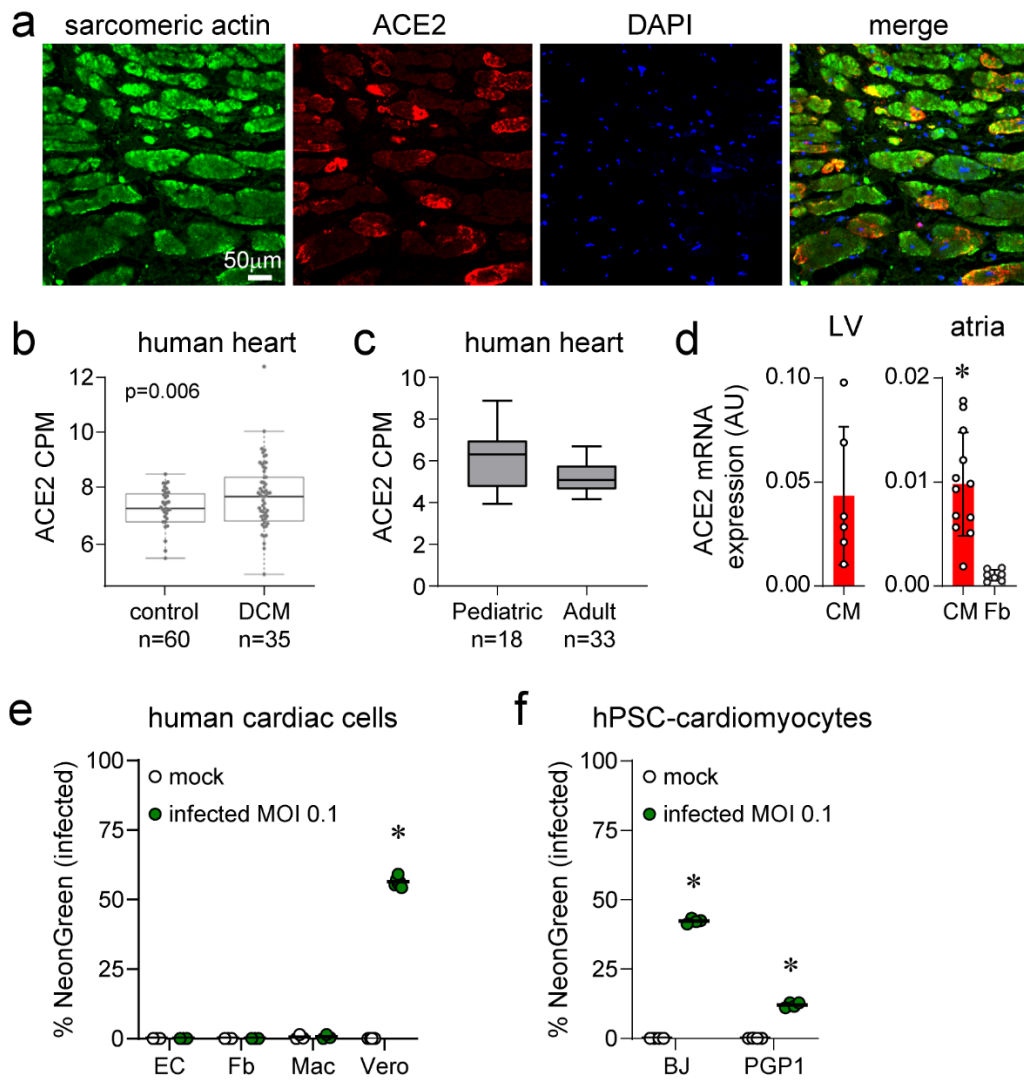
Figure 1: ACE2 is expressed in the human heart and in stem cell derived cardiomyocytes. **a**, Immunohistochemistry of human heart tissue showing ACE2 (red) expression in cardiomyocytes (green, sarcomeric actin). Representative images from 5 analyzed specimens. **b**, RNA sequencing demonstrating ACE2 mRNA expression in myocardial biopsies obtained from adult controls and heart failure patients. Data is displayed as counts per million (CPM). n=18 pediatric, n=33 adult. Each data point indicates an individual sample. n=60 controls, n=35 heart failure. **c**, RNA sequencing demonstrating ACE2 mRNA expression in adult and pediatric heart tissue. Data is displayed as counts per million (CPM). n=18 pediatric, n=33 adult. **d**, Quantitative RT-PCR measurements showing ACE2 mRNA expression in human primary left ventricular (LV), cardiomyocytes (CM), atrial cardiomyocytes, and atrial fibroblasts (Fb). Each data point indicates an individual sample. Error bars denote standard deviation. * $p < 0.05$ compared to atrial fibroblasts (Mann-Whitney test). **e**, Inoculation of primary human endothelial cells (EC), fibroblasts (Fb), and macrophages (Mac) with mock (black) or SARS2-CoV-2-NeonGreen (green, MOI 0.1). Vero cells are included as a positive control. Data is presented as the percent of live cells that express NeonGreen indicating infection. Each data point represents cells isolated from an individual patient sample. Bars denote mean values. * $p < 0.05$ compared to mock infection (Mann-Whitney test). **f**, Inoculation of 2 different hPSC-derived cardiomyocyte lines (BJ, PGP1) with mock (black) or SARS2-CoV-2-NeonGreen (green, MOI 0.1, 1.0). Each data point represents biological replicates. * $p < 0.05$ compared to mock infection (Mann-Whitney test). Bars denote mean values.
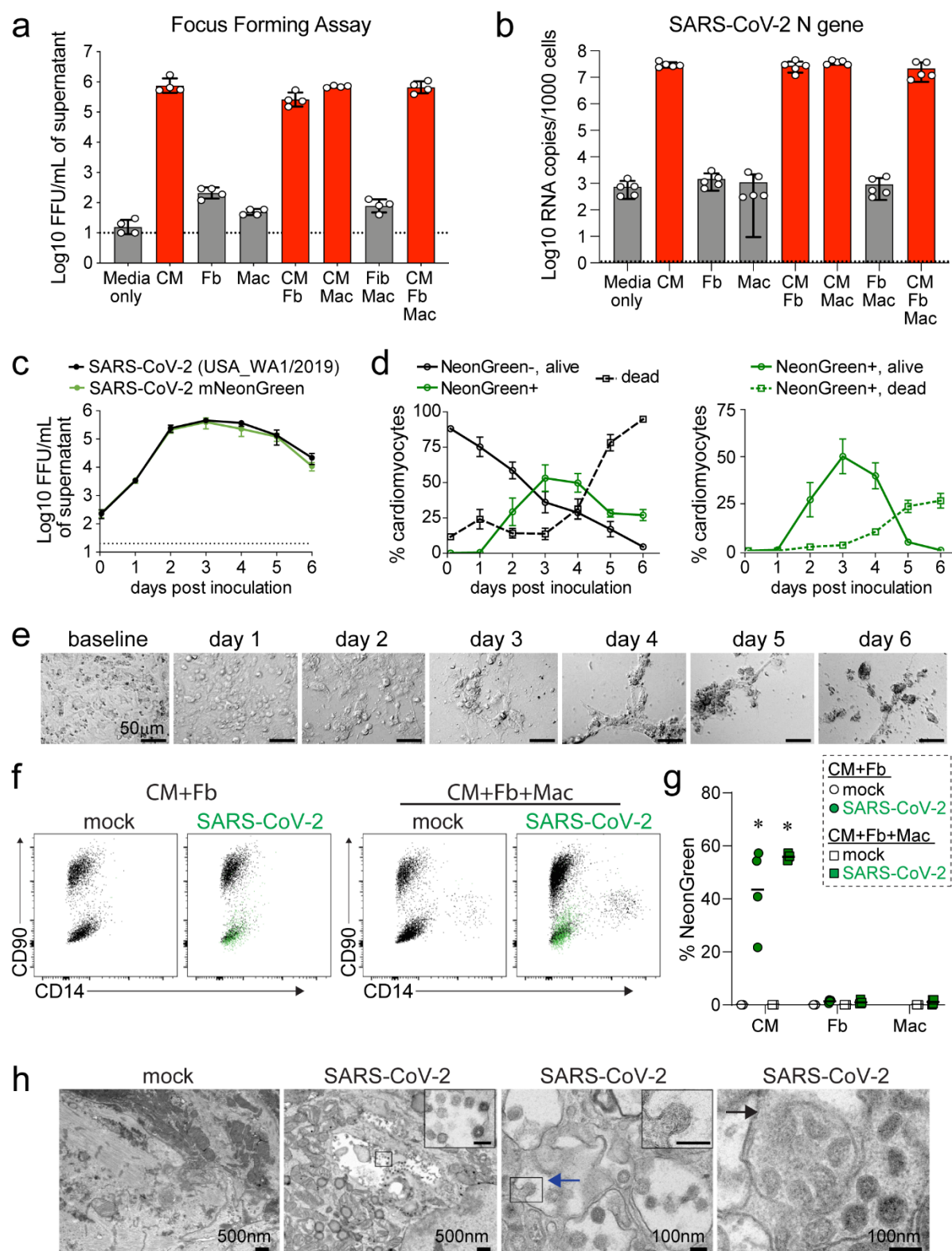
Figure 2: SARS-CoV-2 infects cardiomyocytes. a, Focus forming assay demonstrating production of infectious virus from cultures containing hPSC-derived cardiomyocytes (CM), fibroblasts (Fb), and macrophages (Mac) inoculated with SARS-CoV-2 (MOI 0.1). Media only denotes wells that contain no cells. Assays were performed 3 days following inoculation. Dashed line shows the limit of assay detection. **b**, Quantitative RT-PCR showing viral N gene copies in cultures containing CM, Fb, and Macs inoculated with SARS-CoV-2 (MOI 0.1). RNA was collected 3 days after inoculation. Data points indicate individual samples (n=5, a-b). Bars denote the mean value and error bars indicate standard error of the mean. **c**, Focus forming assay measuring infectious SARS-CoV-2 (wild-type, black; mNeonGreen, green) in supernatant of hPSC-derived cardiomyocytes over time following inoculation (MOI 0.1). Dashed line shows the limit of detection. n=4 per experimental group. Error bars denote standard deviation. **d**, Two-dimensional cultures of hPSC-derived cardiomyocytes were inoculated with SARS-CoV-2 (MOI 0.1) and analyzed for viability (Zombie-Violet) and infection (NeonGreen reporter) as a function of time by flow cytometry. Right plot: viability of NeonGreen positive cells. n=4 per experimental group. Error bars denote standard deviation. **e**, Brightfield microscopy showing cytopathic effect (CPE) in hPSC-derived cardiomyocytes infected with SARS-CoV-2 (MOI 0.1). Representative images from 5 individual samples. **f**, Flow cytometry of two-dimensional tissues containing CM and Fb (left) or CM, Fb, and Mac (right) harvested on day 3 following either mock infection or inoculation with SARS-CoV-2 (MOI 0.1). Representative plot from 4 independent samples. Cardiomyocytes (CD90-CD14-) demonstrated prominent NeonGreen fluorescence (green overlay). NeonGreen signal was not detected in fibroblasts (CD90+CD14-) or macrophages (CD90-CD14+). **g**, Quantification of the percent NeonGreen positive cells from 2-dimensional tissues containing hPSC-CMs and fibroblasts or hPSC-CMs, fibroblasts, and macrophages. Data points indicate individual samples (n=4). * p<0.05 compared to mock infection (Mann-Whitney test). **h**, Transmission electron microscopy micrographs of cardiomyocytes in two-dimensional tissues infected with either mock or SARS-CoV-2 (MOI 0.1). Tissues were harvested on day 3 post-inoculation. Virions are readily apparent. Viral budding (blue arrow) and endosomal compartments filled with virions (black arrow) are denoted. Scale bars in insets are 100 nm. Representative image from 4 independent samples.
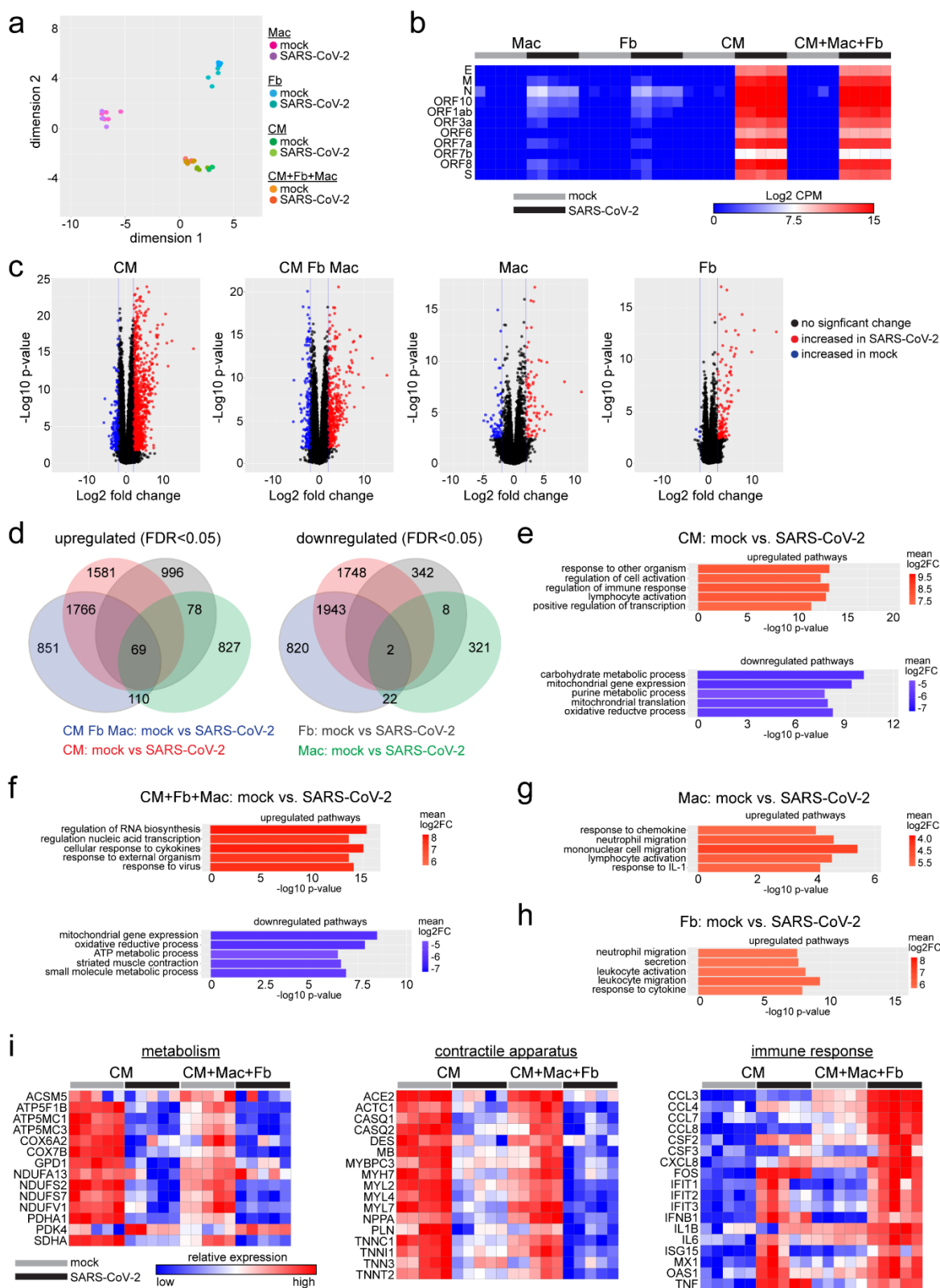
Figure 3: RNA sequencing identified robust viral transcription and activation of innate immune response in hPSC-derived cardiomyocytes and 2D tissues. **a,** MDS plot of RNA sequencing data obtained from mock and SARS-CoV-2 infected (MOI 0.1) hPSC-derived cardiomyocytes (CM), fibroblasts (Fb), macrophages (Mac), and two-dimensional tissues (CM+Fb+Mac) containing all 3 cellular components. Cells and tissues were harvested on day 3 post-inoculation. n=5 per experimental group. **b,** Heatmap of SARS-CoV-2 viral gene expression in each condition. Color scale denotes absolute expression as log2 of counts per million reads (CPM) (blue=0, red=15). **c,** Volcano plots showing differentially expressed genes between mock and SARS-CoV-2 infected conditions. Black: no significant change, Red: upregulated during infection (log2 fold change>2, FDR p-value<0.05), blue: downregulated during infection (log2 fold change<2, FDR p-value<0.05). Data points correspond to individual genes or transcripts. **d,** Venn diagram of genes upregulated and downregulated in each cell type and two-dimensional tissues. Differential expression is based on change relative to corresponding uninfected (mock) samples. **e-h,** GO Pathway analysis of CM (**e**), CM+Fb+Mac (**f**), Mac (**g**) and Fib (**h**) showing top five upregulated (red) and downregulated (blue) pathways in SARS-CoV-2-infected samples compared to mock. Color indicates log2 fold change (log2FC). **i**, Heat maps of selected differentially expressed genes implicated in metabolism (left), contractile apparatus (center) and immune response (right). CM and two-dimensional tissues (CM+Mac+Fb) are displayed. Color scale denotes relative gene expression (high-red, low-blue) across cell types and conditions.
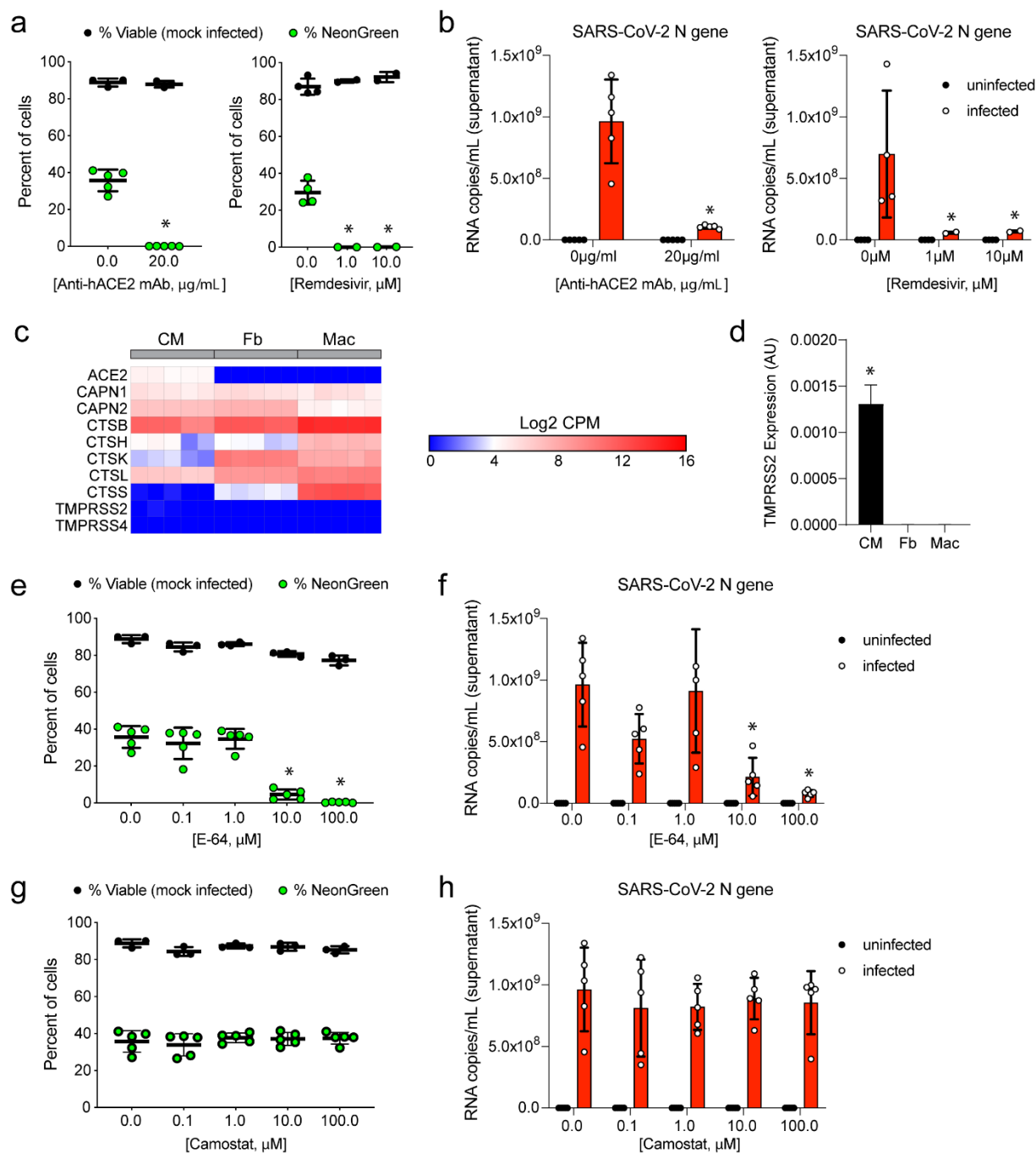
Figure 4. SARS-CoV-2 entry of hPSC-derived cardiomyocytes is mediated by ACE2 and endosomal cysteine proteases. a-b, hPSC-derived cardiomyocytes were infected with mock or inoculated with SARS-CoV-2-mNeonGreen (MOI 0.1). Cells were treated with either vehicle control, anti-human ACE2 neutralizing antibody (Anti-hACE2 mAb, left), or remdesivir (inhibitor of RNA-dependent RNA polymerase, right) at the indicated concentrations. Cells were analyzed by flow cytometry on day 3 post-inoculation for viral infection (NeonGreen, green circles) and viability (Zombie-Violet, black circles) (**a**). The presence of viral RNA in the tissue culture supernatant was also quantified by RT-PCR (**b**). Each data point corresponds to an individual sample/experiment, error bars denote standard error of the mean, *p<0.05 compared to infected cells treated with vehicle control (Mann-Whitney test). **c,** Heatmap of host genes implicated in SARS-CoV-2 cell entry in uninfected hPSC-derived cardiomyocytes (CM), fibroblasts (Fb), and macrophages (Mac). Color scale indicates absolute gene expression levels. **d,** Quantitative RT-PCR for *TMPRSS2* in uninfected hPSC-derived cardiomyocytes (CM), fibroblasts (Fb), and macrophages (Mac). n=5 for each cell type, error bars denote standard error of the mean, *p<0.05 compared to other cell populations (Mann-Whitney test). **e-h**, hPSC-derived cardiomyocytes were mock infected or inoculated with SARS-CoV2-mNeonGreen (MOI 0.1). Cells were treated with either vehicle control, endosomal cysteine protease inhibitor E-64 (**e-f**), or serine protease inhibitor camostat (**g-h**) at the indicated concentrations. Cells were analyzed by flow cytometry on day 3 post-inoculation for viral infection (NeonGreen, green circles) and viability (Zombie-Violet, black circles) (**e,g**). Viral RNA in the tissue culture supernatant was quantified by RT-PCR (**f,h**). Each data point corresponds to an individual sample/experiment, error bars denote standard error of the mean, *p<0.05 compared to infected cells treated with vehicle control (Mann-Whitney test).
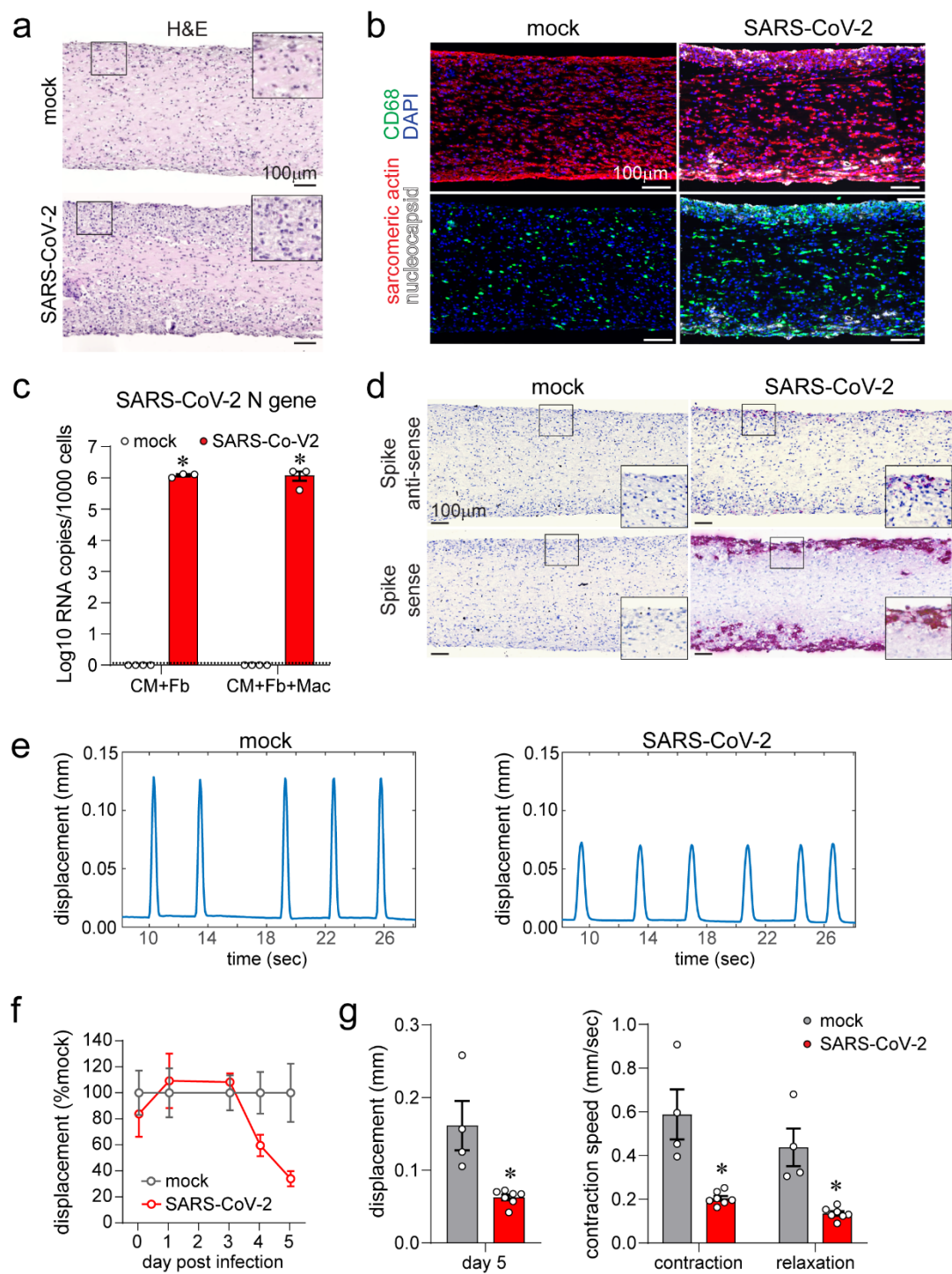
Figure 5. Human engineered heart tissues (EHTs) recapitulate aspects of COVID-19 myocarditis. a, Representative hematoxylin and eosin (H&E) stained histology images of three-dimensional EHTs consisting of hPSC-derived cardiomyocytes (CM), fibroblasts (Fb), and macrophages (Macs) 5 days following mock infection or inoculation with SARS-CoV-2 (MOI 0.1). Insets are high magnification images of the boxed areas. Representative images from 4 independent samples. **b**, Immunostaining of mock or SARS-CoV-2 infected three-dimensional EHTs for sarcomeric actin (cardiomyocytes, red), CD68 (macrophages, green), and nucleocapsid protein (white). EHTs were harvested 5 days after inoculation. Blue: DAPI. Images are representative of 4 independent experiments. Representative images from 4 independent samples. **c,** Quantitative RT-PCR of SARS-CoV-2 N gene expression in EHTs consisting of hPSC-derived cardiomyocytes (CM) and fibroblasts (Fb) or hPSC-derived cardiomyocytes, fibroblasts, and macrophages. EHTs were either mock infected or inoculated with SARS-CoV-2 (MOI 0.1) and harvested 5 days after inoculation. Each data point represents individual samples/experiments. Error bars denote standard error of the mean. Bar height represents sample mean. Dotted line: limit of detection. *$p < 0.05$ compared to uninfected control (mock, Mann-Whitney test). **d,** *In situ* hybridization for SARS-CoV-2 ORF1ab RNA sense and anti-sense strands (red) in EHTs 5 days after mock or SARS-CoV-2 infection (MOI 0.1). Hematoxylin: blue. Representative images from 4 independent specimens. Insets are high magnification images of the boxed areas. **e,** Representative spontaneous beating displacement traces for an infected and an uninfected EHT on day 5 post-infection. Videos used to generate these traces can be found in **Supplemental Videos 1 and 2**. **f,** Displacement (relative to uninfected mock condition) generated by spontaneous beating of EHTs as a function of time following inoculation with SARS-CoV-2 (MOI 0.1). Each data point represents a mean value from 4-7 independent samples (2 independent experiments), error bars denote standard error of the mean. **g,** Quantification of absolute displacement (left) and contraction speed (right) generated by spontaneous beating of EHTs 5 days following mock or SARS-CoV-2 infection (MOI 0.1). Each data point denotes an individual EHT, bar height corresponds to mean displacement, error bars represent standard error of the mean, *$p < 0.05$ compared to mock (Mann-Whitney test).
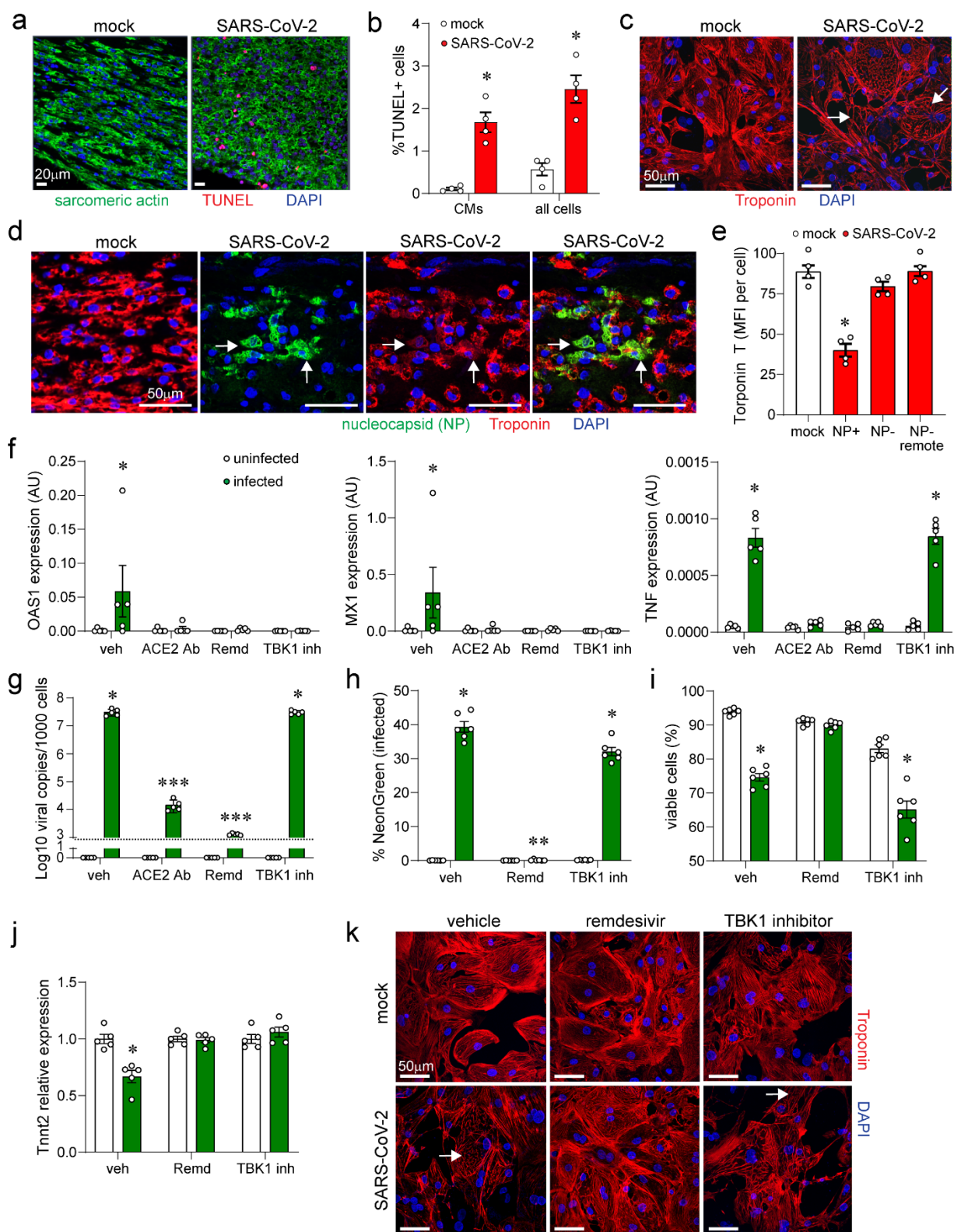
Figure 6. Mechanisms of reduced EHT contractility. a, Combined immunostaining for cardiomyocytes (cardiac actin, green) and TUNEL staining (red) of EHTs (CM+Fb+Mac) 5 days after mock or SARS-CoV-2 infection (MOI 0.1). DAPI: blue. Representative images from 4 independent experiments. **b,** Quantification of cell death (percent of TUNEL-positive cells) in areas of viral infection. Each data point denotes an individual EHT, bar height corresponds to the mean, error bars represent standard error of the mean, *p<0.05 compared to mock (Mann-Whitney test). **c**, Immunostaining of hPSC-derived cardiomyocytes for Troponin T (red) 3 days after inoculation with mock control or SARS-CoV-2-NeonGreen (MOI 0.1). Blue: DAPI. Arrows denote areas of sarcomere disassembly. **d**, Immunostaining of EHTs for Troponin T (red) and SARS-CoV-2 nucleocapsid (green) 5 days after inoculation with mock control or SARS-CoV-2-NeonGreen (MOI 0.1). Blue: DAPI. Arrows denote SARS-CoV-2 nucleocapsid positive cells with reduced Troponin T staining. **e**, Quantification of Troponin T staining in mock (white) and SARS-CoV-2 (red) infected EHTs. NP: nucleocapsid. Data is presented as mean florescence intensity (MFI). MFI was measured in infected (NP+) cardiomyocytes and uninfected (NP-) cardiomyocytes located proximal or remote to areas of infection. Each data point denotes an individual EHT, bar height corresponds to the mean, error bars represent standard error of the mean, *p<0.05 compared to mock (Mann-Whitney test). **f**, Quantitative RT-PCR measuring OAS1, MX1, and TNF mRNA expression in hPSC-derived cardiomyocytes 3 days after inoculation with mock control (white) or SARS-CoV-2 (green, MOI 0.1). Cells were treated with vehicle, ACE2 antibody (ACE2 Ab) (20μg/ml), remdesivir (10μM), or TBK inhibitor (MRT67307, 10μM). Each data point denotes a biologically unique sample, bar height corresponds to the mean, and error bars indicate standard error of the mean. * p<0.05 compared to mock control. **g**, Quantitative RT-PCR of SARS-CoV-2 N gene expression in hPSC-derived cardiomyocytes that were either mock infected (white) or inoculated with SARS-CoV-2 (green, MOI 0.1) and harvested 3 days after inoculation. Cells were treated with vehicle, ACE2 Ab (20μg/ml), remdesivir (10μM), or TBK1 inhibitor (MRT67307, 10μM). Each data point represents individual samples. Error bars denote standard error of the mean. Bar height represents sample mean. Dotted line: limit of detection. *p<0.05 compared to uninfected control. ***p<0.05 compared to uninfected control and vehicle infected (mock, Mann-Whitney test). **h-i**, Flow cytometry measuring the percent of infected (h) and viable (i) hPSC-derived cardiomyocytes following either mock infection (white) or inoculation with SARS-CoV-2 (green, MOI 0.1). Cells were harvested and analyzed 3 days after inoculation. Cells were treated with vehicle, remdesivir (10μM), or TBK1 inhibitor (MRT67307, 10μM). Each data point represents individual samples. Error bars denote standard error of the mean. Bar height represents sample mean. *p<0.05 compared to uninfected control. **p<0.05 compared to vehicle infected (mock, Mann-Whitney test). **j,** Quantitative RT-PCR measuring TNNT2 mRNA expression in hPSC-derived cardiomyocytes 3 days after inoculation with mock control (white) or SARS-CoV-2 (green, MOI 0.1). Cells were treated with vehicle, ACE2 Ab (20μg/ml), remdesivir (10μM), or TBK inhibitor (MRT67307, 10μM). Each data point denotes a biologically unique sample, bar height corresponds to the mean, and error bars indicate standard error of the mean. * p<0.05 compared to mock control. **k**, Immunostaining of hPSC-derived cardiomyocytes for Troponin T (red) 3 days after inoculation with mock control or SARS-CoV-2-NeonGreen (MOI 0.1). hPSC-derived cardiomycoytes were treated with vehicle, remdesivir (10μM) or TBK inhibitor (MRT67307, 10μM). Blue: DAPI. Arrows denote areas of sarcomere disassembly. Merged images can be found in Fig. S8.

a   control autopsy   case 1   case 2   case 3   case 4

b   control autopsy   case 1   case 2   case 3   case 4
spike
nucleocapsid

c   control autopsy   case 1   case 2   case 2
nucleocapsid: white, cardiac actin: red, DAPI: blue

d   control autopsy   case 1   case 2   case 3   case 4
CD68: green, CCR2: red, DAPI: blue

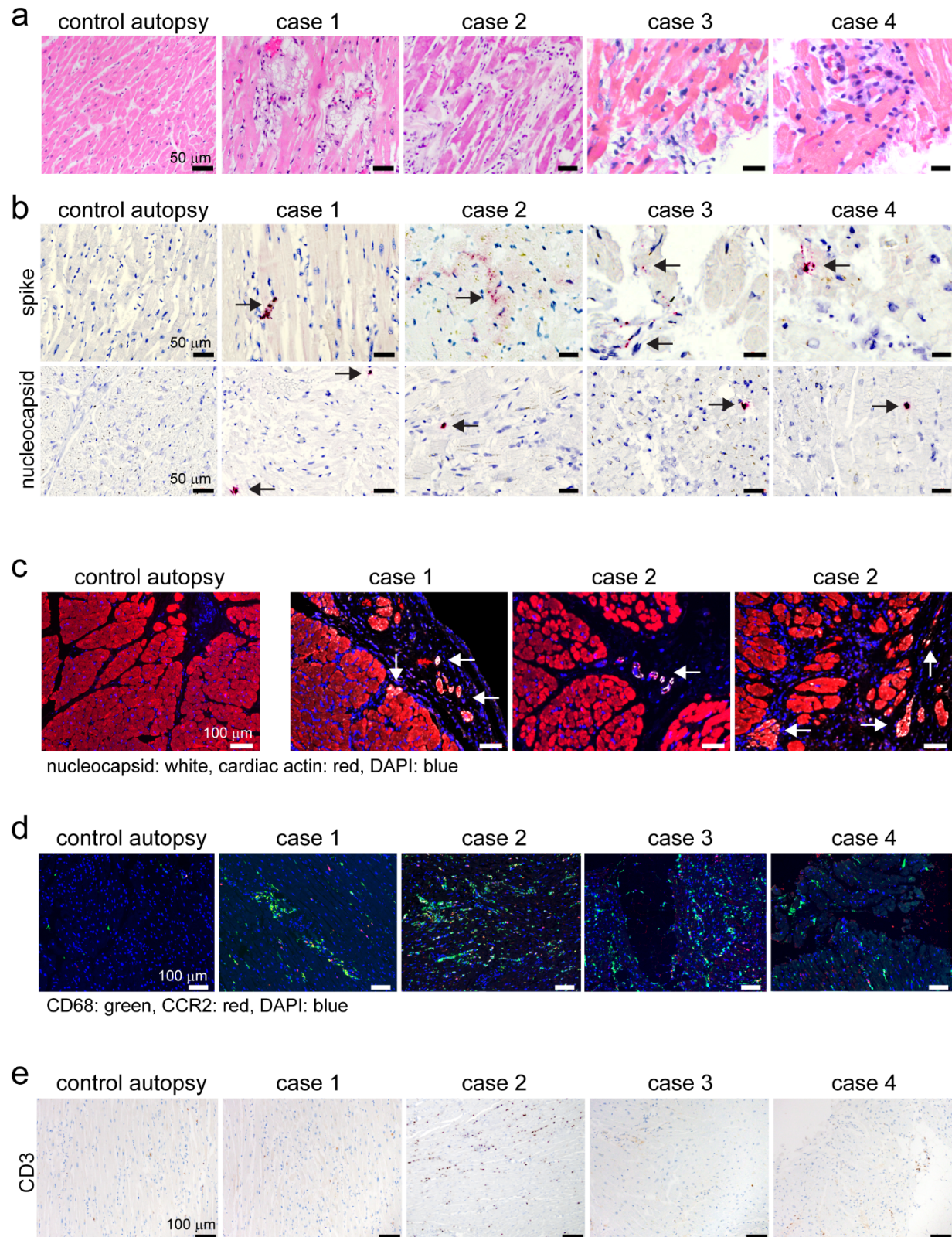e   control autopsy   case 1   case 2   case 3   case 4
CD3

Figure 7. Human autopsy and endomyocardial tissue from patients with suspected COVID-19 myocarditis show evidence of SARS-CoV-2 cardiomyocyte infection. a, Hematoxylin and eosin staining of cardiac autopsy (anterior left ventricular wall) and biopsy samples (right ventricular septum) from subjects without COVID-19 (control case) and patients with a clinical diagnosis of COVID-19 myocarditis (case 1-4). **b,** *In situ* hybridization of cardiac autopsy and biopsy tissue for SARS-CoV-2 spike and nucleocapsid RNA (red) showing evidence of viral infection. Hematoxylin: blue. Arrows denotes viral RNA staining in cells with cardiomyocyte morphology. **c**, Immunostaining of control and COVID-19 myocarditis cardiac autopsy tissue for SARS-CoV-2 nucleocapsid (white) and cardiac actin (red). DAPI: blue. Arrows denotes nucleocapsid staining in cardiomyocytes .**d,** Immunostaining of control and COVID-19 myocarditis cardiac autopsy and biopsy tissue for CD68 (green) and CCR2 (red). DAPI: blue. **e,** Immunostaining of control and COVID-19 myocarditis cardiac autopsy and biopsy tissue for CD3 (brown). Hematoxylin: blue.